Application of a global nonhydrostatic model with a stretched-grid system to regional aerosol simulations around Japan

D. Goto[*1], T. Dai[2], M. Satoh[3,4], H. Tomita[4,5], J. Uchida[3], S. Misawa[3], T. Inoue[3], H. Tsuruta[3], K. Ueda[6], C. F. S. Ng[7], A. Takami[1], N. Sugimoto[1], A. Shimizu[1], T. Ohara[1] and T. Nakajima[3]

[1] National Institute for Environmental Studies, Tsukuba, Japan

[2] State Key Laboratory of Numerical Modeling for Atmospheric Sciences and Geophysical Fluid Dynamics, Institute of Atmospheric Physics, Chinese Academy of Sciences, Beijing, China

[3] Japan Agency for Marine-Earth Science and Technology, Yokohama, Japan

[4] Atmosphere and Ocean Research Institute, University of Tokyo, Kashiwa, Japan

[5] Advanced Institute for Computational Science, RIKEN, Kobe, Japan

[6] Faculty of Engineering, Kyoto University, Kyoto, Japan

[7] Department of Human Ecology School of International Health Graduate School of medicine, University of Tokyo, Tokyo, Japan

*Correspondence to: Daisuke Goto (goto.daisuke@nies.go.jp)

16-2 Onogawa, Tsukuba, Ibaraki 305-8506, Japan

Tel: +81-29-850-2899; Fax: +81-29-850-2580

Abstract

An aerosol-coupled global nonhydrostatic model with a stretched-grid system has been developed. Circulations over the global and target domains are simulated with a single model, which includes fine meshes covering the target region to calculate meso-scale circulations. The stretched global model involves lower computational costs to simulate atmospheric aerosols with fine horizontal resolutions compared with a global uniform nonhydrostatic model, whereas it may require higher computational costs compared with the general regional models, because the stretched-grid system calculates inside and outside the target domain. As opposed to general regional models, the stretched-grid system does require neither a nesting technique nor lateral boundary conditions. In this study, we developed a new-type regional model for the simulation of aerosols over Japan, especially in the Kanto areas surrounding Tokyo, with a maximum horizontal resolution of approximately 10 km. This model usually reproduces temporal variations and their averages of the observed weather around Japan. This model generally reproduces monthly mean distributions of the observed sulfate and SO_2 over East Asia, with the high correlations (R>0.6), but the underestimation of the simulated concentrations by 40% (sulfate) and 50% (SO_2). Their underestimation of the simulated sulfate and SO_2 concentrations over East Asia are strongly affected by their underestimation in China and possibly by the uncertainty of the simulated precipitation around Japan. In the Kanto area, this model succeeds in simulating the wind patterns and the diurnal transitions around the center of the Kanto area, although it is inadequate to simulate the wind patterns and the diurnal transitions at some sites located at the edge

of the Kanto area and surrounded on three sides by mountains, e.g., Maebashi, mainly due to the insufficient horizontal resolution. This model also generally reproduces both diurnal and synoptic variations of the observed and/or a regional aerosol-transport model, WRF-CMAQ, simulated EC, sulfate, and SO_2 concentrations in the Kanto area, especially with their high correlation (R>0.5) at Komae/Tokyo. Although the aerosol module used in this study is relatively simplified compared to the general regional aerosol models, this study reveals that our proposed model with the stretched-grid system can be applicable for the regional aerosol simulation.

1 Introduction

Aerosols can greatly affect regional air quality and contribute to global climate change (Forster et al., 2007). Recently, transboundary aerosol pollution, whereby regions beyond a given country's borders are affected by the aerosols generated in that country, has been of increasing concern (Ramanathan et al., 2008; Yu et al., 2012). The ongoing rapid economic growth in developing countries has the potential to exacerbate this issue (UNEP and WMO, 2011). Air pollution generated by aerosols is a critical public health issue due to the deleterious effects of these particles on human health (Dockery et al., 1993; Pope et al., 2009). Aerosols, which scatter and absorb solar radiation and act as cloud condensation nuclei, can directly and indirectly change the Earth's radiation budget. The majority of aerosols are emitted from localized areas, which are referred to as hotspots, such as megacities and biomass-burning regions, and are spread throughout the world via atmospheric transport (e.g., Ramanathan et al., 2008). Therefore, global aerosol-transport models should consider the important regional-scale characteristics of aerosol hotspots to reliably estimate their impacts on air quality and climate change.

Most existing global aerosol-transport models do not address the spatial variability of aerosols in the vicinity of hotspots due to their coarse horizontal resolution of 100–300 km (Kinne et al., 2006; Textor et al., 2006). In addition, global aerosol-transport models with coarse resolutions frequently adopt a spectral transform method with a hydrostatic approximation to effectively calculate atmospheric dynamics. This spectral transform method is less effective than the grid-point method (Stuhne and Peltier, 1996; Taylor et al., 1997; Randall et al., 2000) for high horizontal resolutions (Tomita et al., 2008). Models that employ the grid-point method flexibly define grid points to enable an adaptive focus on study regions. Thus, global models based on the grid-point method seem most appropriate for use in simulating aerosol transport from hotspots to outflow regions.

For this purpose, we utilized the global Nonhydrostatic Icosahedral Atmospheric Model (NICAM) developed by Tomita and Satoh (2004) and Satoh et al. (2008). NICAM has been employed for the global simulation of atmospheric processes with high-resolution grid spacing, whose size is comparable to the typical deep convective cloud scale. Miura et al. (2007) performed a one-week computation with a horizontal resolution of 3.5 km using the Earth Simulator at the Japan Agency for Marine-Earth Science and Technology (JAMSTEC) to successfully simulate a Madden-Julian Oscillation (MJO) event. Suzuki et al. (2008) implemented an aerosol transport model named the Spectral Radiation-Transport Model for Aerosol Species (SPRINTARS; Takemura et al., 2005) in NICAM (we refer to this aerosol-coupled model as NICAM-SPRINTARS) and performed a one-week simulation with a horizontal resolution of 7 km using the Earth Simulator. Although these global, highly resolved calculations are promising with regard to long-term climate simulations for decades, their requirement of vast computer resources substantially limits their use in short-duration and/or case-specific simulations due to the current limitations of computational resources. To overcome this limitation, we adopt a compromise approach based on a new grid transformation named the stretched grid system, which was developed and implemented in NICAM by Tomita (2008a) for computationally effective simulations in the target region (see, also, Satoh et al. 2010). We applied this approach to NICAM-SPRINTARS, which we named Stretch-NICAM-SPRINTARS, to calculate aerosol transport processes with high horizontal resolutions over aerosol source regions.

In this study, we focused on Japan, especially the Kanto region surrounding Tokyo (Figure 1), because the Kanto region living more than 30 million people is one of the largest megacities in the world. In Japan, a monitoring system for the air pollution, e.g., PM2.5 (aerosol particles with diameters less than 2.5 μm) and SO_2, has been operated by the Japanese government. Inorganic ions, mainly sulfate, have been measured over Japan and other Asian countries under EANET (Acid Deposition Monitoring Network in East Asia; http://www.eanet.asia/index.html). Measurements of carbonaceous aerosols were limited, with the exception of intensive measurements (Fine Aerosol Measurement and Modeling in Kanto Area, FAMIKA) in the Kanto region during summer 2007 (Hasegawa et al., 2008; Fushimi et al., 2011). For the model evaluation using these measurements, we simulated aerosol spatial distributions during August 2007 using Stretch-NICAM-SPRINTARS with a horizontal resolution of approximately 10 km over the Kanto region. Because the model framework of Stretch-NICAM-SPRINTARS is identical to that of globally uniformed grid simulation (we named it Global-NICAM-SPRINTARS), with the exception of the grid configuration, and involves lower computational costs than global simulations, the investigation of the model performance of Stretch-NICAM-SPRINTARS can be simply and effectively extended to improve the original NICAM-SPRINTARS with globally uniform high resolution for near-future simulations. To evaluate aerosol simulations with the stretched-grid system, in this study we also conducted Global-NICAM-SPRINTARS, but with relatively low resolution (approximately 100 km) due to the limited computational resources. The model intra-comparison approach, with the exception of the grid system and the spatial resolution, is very meaningful to investigate impacts of the stretched-grid system on the aerosol simulations. In addition, Stretch-NICAM-SPRINTARS can be a new-type model that is also applicable for a regional simulation of aerosols, because it focuses on a specific regional domain without require a nesting technique nor boundary conditions, unlike general regional models.

For the model evaluation in the target Japan, we mainly focused on a representative primary aerosol, i.e., elemental carbon (EC), and a representative secondary aerosol, i.e., sulfate. EC is directly emitted from anthropogenic combustion processes, and is a good indicator to monitor the transport pattern. The global and regional modelings for sulfate, which is formed from SO_2 in the atmosphere, are more deeply understood compared to modelings for the other secondary aerosols such as nitrate and organic aerosols (e.g., Barrie et al., 2001; Holloway et al., 2008; Hallquist et al., 2009; Morino et al., 2010a, 2010b). In addition, sulfate is the largest contributor to the total secondary inorganic aerosols (e.g., Zhang et al., 2007), and the sulfate mass concentrations are larger than that the nitrate ones in August 2007 over the Kanto area (Morino et al., 2010c). Originally, these basic components (EC and sulfate) are suitable for the evaluation in this study, primarily because the stretched-grid system was applied to the simulations of atmospheric pollutants over the land in the mid-latitude bond for the first time and secondly because the original SPRINTARS is more simplified compared to conventional regional aerosol models.

This paper is organized as follows: the model framework of NICAM and SPRINTARS and the experimental design are described in Section 2. We show two model results; (1) Stretch-NICAM-SPRINTARS with glevel-6, in which “glevel” is the number of divisions of an icosahedron used to construct the horizontal grid, (hereafter referred to as the “NICAM-g6str” model) and (2) Global-NICAM-SPRINTARS with glevel-6 (hearafter referred to as the “NICAM-g6” model). In Section 3, the model results are validated using in-situ measurements in terms of meteorological fields including precipitation and aerosol species, especially EC, sulfate and SO_2. For the model evaluation of chemical species, we also made use of results in a regional aerosol model, the Community Multiscale Air Quality (CMAQ) driven by the Weather Research and Forecasting (WRF) model named WRF-CMAQ, shown by Shimadera et al. (2013). We also present the validation of total aerosol amounts, i.e., PM2.5, and aerosol optical product, i.e., extinction for spherical aerosols. Finally, the conclusions are summarized in Section 4.

2 Model description

2.1 Nonhydrostatic Icosahedral Atmospheric Model (NICAM)

NICAM, which employs an icosahedral grid-point method with a nonhydrostatic equation system (Tomita and Satoh, 2004; Satoh et al., 2008, 2014), is run with a maximum horizontal resolution of 3.5 km (Tomita et al. 2005; Miura et al., 2007) and can be applied to a transport model of aerosols and gases as a conventional atmospheric general circulation model (Suzuki et al., 2008; Niwa et al., 2011; Dai et al., 2014a, 2014b; Goto, 2014). NICAM can also be employed for regional-scale simulations by adopting a stretched-grid system (Tomita, 2008a; Satoh et al., 2010). The stretched icosahedral grid was developed from a general grid transformation method, i.e., the Schmidt transformation method, for a horizontal grid system on a sphere. In the Schmidt transformation, the grid interval on a sphere lacks uniformity with a finer horizontal resolution close to the center of the target region. Tomita (2008a) showed that the Schmidt transformation minimizes potential errors involving the isotropy and homogeneity of the target region. The stretched-grid system can solve the main problems associated with commonly used regional models, which occur from artificial perturbations near boundary areas in cases where meteorological and aerosol fields are prescribed. In addition, the computational cost of the stretched-grid system is substantially lower than that of a global calculation under the same horizontal resolution in the target region. For example, when the globally uniform grid with a maximum horizontal resolution of 10 km is applied to the global simulation, the minimum required theoretical computational cost is 64-256 times higher than the cost of the stretched-grid system in this study. Compared to conventional regional models, the computational cost may increase because the stretched-grid system requires the calculation outside the target domain. Furthermore, the model framework of the stretched global model is identical to that of the uniformed global model without special modifications, whereas the model framework of regional models is usually different from that of global models. These advantages can facilitate additional developments for global simulations by testing a new scheme with minimal computational cost. Compared with general regional models, the stretched-grid system is more suitable for the future study, which aimed to extend its use to the global uniform high-resolution NICAM-SPRINTARS.

In this study, we adopt the stretched-grid system to focus on the Kanto region, including Tokyo, using glevel-6 resolution and the stretched ratio of 100 (we call it NICAM-g6str), which is the ratio of the largest horizontal grid spacing located on the opposite side of the earth from Tokyo to the smallest horizontal grid spacing near Tokyo. As a result, a minimum horizontal resolution of 11 km around the center (140.00°E, 35.00°N) was used. NICAM implements comprehensive physical processes of radiation, boundary layer and cloud microphysics. The radiation transfer model is implemented in NICAM with the k-distribution radiation scheme MSTRN, which incorporates scattering, absorption and emissivity by aerosol and cloud particles as well as absorption by gaseous compounds (Nakajima et al., 2000; Sekiguchi and Nakajima, 2008). The vertical turbulent scheme comprises the level 2 scheme of turbulence closure by Mellor and Yamada (1974), Nakanishi and Niino (2004, 2009) and Noda et al. (2009). The cloud microphysics consist of the six-class single-moment bulk scheme (water vapor, cloud water, rain, cloud ice, snowflakes and graupel) (Tomita, 2008b). Based on our experience in previous studies, we did not employ cumulus parameterization in this study (e.g., Tomita et al., 2005; Sato et al., 2009; Nasuno, 2013). The topography used in this study is based on GTOPO30 (the horizontal resolution is 30 arc seconds, that is approximately 1 km) courtesy of the U.S. Geological Survey. The vertical coordinates system adopts Lorenz grid and z* (terrain-following) coordinates with the 40 layers of z-levels and model top of 40 km height (Satoh et al., 2008).The timestep was set to 20 seconds.

2.2 SPRINTARS

Based on the approach of Suzuki et al. (2008), the three-dimensional aerosol-transport model—Spectral Radiation-Transport Model for Aerosol Species (SPRINTARS; Takemura et al., 2000, 2002, 2005; Goto et al. 2011a,b,c)—was coupled to NICAM in this study. The SPRINTARS model calculates the mass mixing ratios of the primary tropospheric aerosols, i.e., carbonaceous aerosol (EC and OC, organic carbon), sulfate, soil dust, sea salt and the precursor gases of sulfate, namely, SO_2 and dimethylsulfide (DMS). The aerosol module considers the following processes; emission, advection, diffusion, sulfur chemistry, wet deposition and dry deposition, including gravitational settling. For carbonaceous aerosols, the 50% mass of EC from fossil fuel sources is composed of externally mixed particles, whereas other carbonaceous particles are emitted and treated as internal mixtures of EC and OC (EC-OC internal mixture). Biogenic secondary organic aerosols (SOAs) from terpenes are treated but are greatly simplified by multiplying a conversion factor to the terpenes emission (Takemura, 2012). In addition, anthropogenic SOAs from toluene and xylene are disregarded in this study. The bulk mass concentrations of EC, OC, and sulfate are calculated by single-modal approach, which means that the SPRINTARS model does not explicitly treat aerosol dynamic processes such as coagulation and condensation. The particle size distribution of the dry particles are prescribed in a logarithmic normal size distribution with dry mode radii of 18, 100, 80 and 69.5 nm, for pure EC, EC-OC internal mixture, biogenic SOA and externally mixed sulfate, respectively (Goto et al., 2011a). The hygroscopicities, densities and refractive indices for the aerosols are set to the same values used by Takemura et al. (2002) and Goto et al. (2011a). The combinations of the pre-calculated cross-sections of the extinction and simulated mixing ratios for each aerosol species provide the simulated aerosol extinction coefficient for each timestep of the model (Takemura et al., 2002). The sulfur chemistry in SPRINTARS considers only three chemical reactions to form sulfate through gas-phase oxidation of SO_2 by hydroxyl radical (OH) and aqueous-phase oxidation by ozone and hydrogen peroxide. The large part of SO_2 are emitted from fossil fuel combustion, biomass burning, and volcano eruption, whereas some of SO_2 are formed from the oxidation of DMS, which is emitted naturally from marine phytoplanktons. The numerical solution in the oxidations adopts an approximation in a quasi first-order reaction using the same integrated time resolution as that of the dynamic core. The pH value in the aqueous-phase is fixed at 5.6, because the SPRINTARS model treats limited ions in the aqueous-phase (e.g., Takemura et al., 2000). The oxidant distributions (OH, ozone and hydrogen peroxide) were offline provided by a chemical transport model. The atmospheric removal of aerosols in SPRINTARS includes wet (due to rainout and washout) and dry (due to turbulence and gravity) deposition processes, whereas those of SO_2 only include rainout and dry deposition by turbulence. In the cloudy grid, the mass fractions of sulfate out of the cloud droplets to the mass of sulfate in the grid were fixed at 0.5, whereas the fractions for SO_2 were determined by Henry's law (Takemura et al., 2002). As for pure EC, EC-OC internal mixture, and biogenic SOA, the mass fractions were fixed at 0.1, 0.3, and 0.3, respectively. Because the SPRINTARS model does not predict the mass mixing ratio of the chemical tracers inside the clouds, it assumes that the tracers inside the clouds are evaporated from the clouds at one timestep. In this study, the particle mass concentrations for diameters less than 2.5 μm (defined as PM2.5) are calculated by summing EC, organic matter by multiplying OC by 1.6 (Turpin and Lim, 2001), sulfate and ammonium aerosols. Because this model cannot directly predict ammonium compounds, it is assumed that all sulfate is the form of ammonium sulfate, so that their concentration was estimated by multiplying the mass concentration of sulfate by 0.27, which is the molar ratio of ammonium ion to ammonium sulfate. The nitrate in this study is disregarded, primarily because the main objective in this study is modeling of sulfate as a representative secondary aerosols and secondly because the nitrate mass concentrations are lower than the sulfate ones with the target of August 2007 in Japan (Morino et al., 2010c).

2.3 Design of the experiments

The target period comprises one month in August 2007, in which an intensive measurement of aerosol chemical species was conducted under Project FAMIKA (Hasegawa et al., 2008; Fushimi et al., 2011). The six-hour meteorological fields (wind and temperature) were nudged above a height of 2 km using NCEP-FNL reanalysis data (http://rda.ucar.edu/datasets/ds083.2/). The one-day sea surface temperature was also nudged using the NCEP-FNL data. The initial conditions were prescribed by the NCEP-FNL data for the meteorological fields and the one and a half months spinup results of the Stretch-NICAM-SPRINTARS model for the aerosol fields, respectively.

The emission inventories of anthropogenic EC, OC and SO_2 in this experiment were prepared by EAGrid2000 with a horizontal resolution of 1 km over Japan (Kannari et al., 2007), REAS version 2 with a horizontal resolution of 0.25° over Asia (Kurokawa et al., 2013) and the AeroCom inventory with a horizontal resolution of 1° over other areas of the world (Diehl et al., 2012). Because EAGrid2000 does not explicitly estimate EC and OC inventories, we estimated the inventories to be consistent with those from previous studies (Morino et al., 2010a,b; Chatani et al., 2011) by modifying the PM2.5 inventory of EAGrid2000 using scaling factors of EC/PM2.5 and OC/PM2.5 based on sources. These inventories of anthropogenic EC and SO_2 in 2007 are described in Figure 2. The emissions of SO_2 from volcanoes in Japan, such as Miyakejima and Sakura-jima, were obtained from statistical reports (http://www.seisvol.kishou.go.jp/tokyo/volcano.html) by the Japan Meteorological Agency (JMA). In this study, the distributions of three hourly averaged monthly oxidants (OH, ozone and hydrogen peroxide) were derived from a global chemical transport model (CHASER) coupled to the Model for Interdisciplinary Research on Climate (MIROC), named MIROC-CHASER, with the spatial resolution of 2.8° by 2.8° (Sudo et al., 2002).

To evaluate model performances in the stretched-grid system, we also simulated NICAM-SPRINTARS with the globally uniformed grid simulation in glevel-6 resolution (the horizontal resolution is set to 110 km and we call it NICAM-g6). Global-NICAM-SPRINTARS with relatively low resolution has been applied to aerosol simulations and well compared with in-situ measurements and satellite remote sensing (Dai et al., 2014a; Goto, 2014). Apart from the NICAM-g6str simulation, in the NICAM-g6 simulation, the cloud physics apply both the prognostic Arakawa-Schubert-type cumulus convection scheme (Arakawa and Schubert, 1974) and the diagnostic large-scale clouds described by Le Treut and Li (1991). The large-scale cloud module is based on single moment bulk scheme for cloud mixing ratio. The precipitation rate is parameterized by Berry (1967). Except for the grid system and the horizontal resolution (which determines the module of the cloud physics), Global-NICAM-SPRINTARS was identical to Stretch-NICAM-SPRINTARS. Therefore, the comparison between NICAM-g6str and NICAM-g6 led to clarify impacts of the horizontal resolution on the aerosol distribution.

2.4 Observation

In this study, we focused on the aerosol chemical component of EC as the primary particle and sulfate as the secondary particle. To evaluate the model results over the Kanto region, we used observations of the surface mass concentrations of EC and sulfate in four cities under Project FAMIKA: Maebashi/Gunma (139.10°E, 36.40°N), Kisai/Saitama (139.56°E, 36.09°N), Komae/Tokyo (139.58°E, 35.64°N) and Tsukuba/Ibaraki (140.12°E, 36.05°N). The EC particles in PM2.5 were collected every six hours with quartz fiber filters and analyzed with the thermal/optical method according to the IMPROVE protocol (Chow et al., 2001). The sulfate particles in PM2.5 were also collected every six hours with Teflon filters and analyzed by ion chromatography. In addition to the limited FAMIKA dataset, we utilized measurements taken by the EANET (Acid Deposition Monitoring Network in East Asia; http://www.eanet.asia/index.html) and the 4th national survey report of acid rain over Japan in fiscal year 2007 (http://tenbou.nies.go.jp/science/institute/region/journal/JELA_3403041_2009.pdf) to assess the monthly mean concentrations of sulfate and SO_2 at Japanese and Korean sites. We also obtained Chinese measurements by *Zhang et al*. [2012], as part of the Chinese Meteorological Administration Atmosphere Watch Network (CAWNET). To validate the concentration of SO_2 for the Kanto region, we accessed monitoring stations operated by Japanese and local governments.

In the validation of the meteorological fields simulated by NICAM-g6str and NICAM-g6, we used meteorological fields (wind and temperature) reanalyzed by NCEP-FNL over East Asia. In the Kanto region, we obtained measurements for the meteorological parameters (temperature, relative humidity (RH) and wind) at or near the 7 sites of Project FAMIKA and additional cities: Tsuchiura/Ibaraki (140.20°E, 36.07°N), which is the city nearest to Tsukuba; Yokohama/Kanagawa (139.64°E, 35.45°N); Chiba/Chiba (140.12°E, 35.62°N); Adachi/Tokyo (139.82°E, 35.77°N); and Machida/Tokyo (139.43°E, 35.53°N), which is the city nearest to Komae, as shown in Figure 1(b). For precipitation, we used a measurement taken by the Automated Meteorological Data Acquisition System (AMeDAS) at 21 sites over Japan including the following 10 Kanto's sites: Yokohama; Chiba; Tsukuba; Tokyo, which is near Adachi; Maebashi; Huchu, which is near Machida; Konosu, which is near Kisai; Abiko (140.11°E, 35.60°N); Saitama (139.59°E, 35.88°N); and Nerima (139.59°E, 35.74°N) (Figure 1). To evaluate the spatial patterns of the precipitation obtained by NICAM-g6str and NICAM-g6, we used the quantities of the monthly mean precipitation around Japan that were derived from the Global Satellite Mapping of Precipitation (GSMaP; Okamoto et al., 2005; Kubota et al., 2007; Aonashi et al., 2009; Ushio et al., 2009) and the Meso Scale Model (MSM) developed by the JMA for rain forecast (Saito et al., 2006). The results by MSM are generally higher accurate than those in GSMaP, although the covering area in MSM is limited around Japan.

To evaluate the quantities of the total aerosol amounts, such as PM2.5, we compared the simulated PM2.5 concentrations with the observations at the 18 sites including the FAMIKA sites and other monitoring stations operated by the Japanese and local governments (Figure 1). The PM2.5 concentrations were continuously observed using tapered element oscillating microbalance (TEOM) with Series 1400a Ambient Particulate Monitor. The instruments are controlled under the temperature of 50 °C, to minimize the influence of change in the ambient temperature and RH. However, it includes large uncertain due to the difficulty in completely eliminate the water content attached to aerosols and lacks of the calibration of the instrument in some of sites. Nevertheless, the observed PM2.5 concentrations with hourly time resolution were still useful to validate the model results.

In Tsukuba and Chiba, light detection and ranging (LIDAR) measurements operated by the National Institute for Environmental Studies (NIES) of Japan were also available (Sugimoto et al., 2003; Shimizu et al., 2004). The LIDAR unit measured vertical profiles of the backscattering intensity at 532 and 1064 nm and the depolarization ratio at 532 nm. The backscattering intensity was converted to the extinction coefficient, and the depolarization ratio distinguished the extinction between spherical and non-spherical particles. In this study, we only used vertical profiles of the extinction for spherical particles. A detailed algorithm was provided by Sugimoto et al. (2003) and Shimizu et al. (2004).

3 Validation of Stretch-NICAM-SPRINTARS

3.1 Meteorological fields

So far, the stretched-grid system was mainly applied to the simulations of tropical cyclones or tropical convective clouds with small domain over oceans for the short-term period (less than several days) (e.g., Satoh et al., 2010; Arakane et al., 2014). In this study, we focused on the air pollution around Japan (for the longer period). Therefore, we first focused on the general circulation of the basic meteorological fields over the large domain, which can affect the air pollution over Japan. Figure 3 shows temperature and winds near the surface and the model height of approximately 5 km over Asia region (100°E-170°E, 10°N-50°N). In August, North Pacific High (or Ogasawasa High) mainly brings clear weather around Japan. A frequency of the precipitation is usually limited, but a total amount of the monthly mean precipitation is not small, because of typhoons and shower rain. In the focusing region, the general meteorological fields simulated by NICAM-g6str and NICAM-g6 are comparable to those obtained by NCEP-FNL. The absolute biases in the temperature between NICAM-g6str and NCEP-FNL or between NICAM-g6 and NCEP-FNL are within 1.5 °C at the surface and the height of 5 km. Around the Japanese Alps, however, the NICAM-g6str-simulated temperature is lower than the NCEP-FNL-estimated one by at most 2.5 °C, because of the differences in the resolved topography due to the different spatial resolution between NICAM-g6str and NCEP-FNL. As for wind, western winds over the northeastern part of Japan in both NICAM-g6str and NICAM-g6 are stronger compared to those in NCEP-FNL. With the exception of this bias, the performances of both NICAM-g6str and NICAM-g6 are good. Therefore, it is concluded that the stretched-grid systems does not affect the general circulations under the nudging technique in this study.

To evaluate the model performances of the six-hourly mean concentrations of aerosol chemical species and SO_2 over the main target region, i.e., Kanto area, we used the six-hourly instant observations of temperature, RH, wind and precipitation at each station over the Kanto area shown in Figure 1. The results and summary are shown in Figures 4 to 7 and Table 1. The NICAM-g6 results, especially in terms of diurnal variations, tend to be far from the observations compared to the NICAM-g6str results, because NICAM-g6, with the horizontal resolution of approximately 100 km, does not fully resolve the topology over the Kanto area. Figure 4 illustrates the temporal variations of temperature at a height of 2 m. The temporal variations in the NICAM-g6str-simulated temperature are generally comparable to those in the observed temperatures with root-mean-square-error (RMSE) values of less than 3°C, with the exception of the results obtained for Maebashi and Machida. At these two sites, the mean values of the NICAM-g6str-simulated temperatures are lower than those of the observed temperatures by a maximum of 3.6°C. The correlation coefficients (R) between NICAM-g6str and the observation range from 0.7–0.9, whereas the R between NICAM-g6 and the observation range from 0.7-0.8, as shown in Table 1. Figure 5 shows the temporal variations in RH at a height of 2 m. The temporal variations in the NICAM-g6str-simulated RH are similar to the observations, with the RMSEs in the range of 10–15%. In contrast, the NICAM-g6-simulated RH is overestimated compared to the observations, with the RMSEs in the range of 16–26%. The R values of RH between the simulation (both NICAM-g6str and NICAM-g6) and observations are approximately 0.6–0.8 (Table 1).

The temporal variations in the wind direction and speed simulated by NICAM-g6str are compared with the observations in Figures 6 and 7. Near the southern part of the Kanto area (Yokohama, Tsuchiura, Adachi and Machida), with the exception of Chiba, the NICAM-g6str-simulated wind direction is generally comparable to the observations, with a slight overestimation of the both NICAM-g6str and NICAM-g6 simulated wind speed compared with the observations. At these four sites, the R and RMSE values in NICAM-g6str range from approximately 0.5–0.7 and approximately 1.7–2.3 m/s, respectively. In Chiba located near the ocean, the R value of wind speed between NICAM-g6str and the observation is 0.41, whereas the NICAM-g6str-simulated wind directions generally agree with the observations. Conversely, at Maebashi and Kisai, the daily variations in the both NICAM-g6str and NICAM-g6 simulated wind directions differ significantly from those in the observations, in which the southern winds and northern winds frequently occur during the day and night, respectively, for example, during August 5–12. At these two sites, the NICAM-g6-simulated wind direction and speed is not closer to the observations compared to those obtained by NICAM-g6str. The R value for wind speed between the NICAM-g6str and the observations at these sites is estimated to be approximately 0.2. The observed southeasterly wind is long sea breeze toward Maebashi Plateau surrounded on three sides by mountains around Maebashi. The observed winds are caused by daytime meso-scale thermal lows developed over the central Japan covering the Japanese Alps (Kuwagata and Sumioka, 1991). The Japanese Alps with the highest terrain in Japan can affect the local meteorological fields even around 100-200 km away (Kitada et al., 1998). Therefore, it suggests that the horizontal resolution in this study using NICAM-g6str (10 km over the Kanto area) does not fully resolve the complex terrains of the Japanese Alps and the Maebashi plateau. Therefore, it suggests that it is inadequate to simulate the wind patterns and the diurnal transitions near high mountains around the Kanto area, whereas it is adequate to simulate them around the center of the Kanto area.

Figures 8-10 show comparisons of NICAM-g6str and NICAM-g6 simulated precipitation with the observations. Figure 8 compares the simulated precipitation with the MSM and GSMaP derived results. During the early August 2007, mainly due to passing of a typhoon over the western Japan, Okinawa, and Korea, the August mean precipitation in the western Japan is larger than that in the eastern Japan, especially the Kanto area. The monthly mean precipitation is estimated to be more than 200 mm/month over the western Japan, whereas that is estimated to be less than 50 mm/month over the eastern Japan. The horizontal patterns of the precipitation obtained by NICAM-g6str in East China Sea, Sea of Japan near the Japan coast, and Korea are closer to those derived from MSM and GSMaP than those obtained by NICAM-g6. In the Kanto area, however, the NICAM-g6str-simulated precipitation with the range of

50-200 mm/month is overestimated compared to the MSM and GSMaP results. The NICAM-g6-simulated precipitation over the Kanto area with the range of 100-200 mm/month is also much overestimated. In Figure 9 showing the temporal variations in the amount of precipitation per day at 21 Japanese sites, the observed precipitation is extremely limited during August 7-19 in the Kanto area. In other regions, the magnitude of the precipitation is strong, although the precipitation is sporadic. In terms of the frequency of the precipitation, the NICAM-g6str performance is better than the NICAM-g6 one. Figure 10 illustrates the predictive value of daily precipitation, defined as the ratio of the number of days where the model correctly predicts the weather (less than 1 mm/day or more than 1 mm/day) to the number of the whole days. In the NICAM-g6str results, the predictive values at most of sites over the Kanto area and four sites over the non-Kanto area such as Nagoya and Osaka are calculated to be more than 85%. The predictive values obtained by NICAM-g6str are mostly higher than those obtained by NICAM-g6. During the rainy days such as August 20, 22 and 23 over the Kanto area, both NICAM-g6str and NICAM-g6 capture the precipitation, whereas NICAM-g6str reproduces greater amounts of the precipitation and NICAM-g6 reproduces longer periods and larger areas compared to the observations. NICAM-g6str does not always capture a sudden shower, as general meteorological models have difficulties in predicting this type of precipitation system (e.g., Kawabata et al., 2011). To increase the accuracy of such precipitation, more sophisticated cloud-microphysics model, e.g., NICAM-NDW6 model proposed by Seiki and Nakajima (2014) based on the double-moment bulk scheme with six water categories, may be required. In the western Japan, during the rainy days, e.g., August 22-23, both NICAM-g6str and NICAM-g6 usually capture large-scaled precipitation (Figure 9). Overall, NICAM-g6str usually reproduces the observed weather in the target regions and periods, whereas NICAM-g6 does not capture general feature such as the sporadic precipitation.

3.2 Aerosol fields

3.2.1 Evaluation of chemical species

Figures 11, 12, and 13 illustrates the temporal variations in the surface EC, sulfate, and SO_2 concentrations at the four stations (Maebashi, Kisai, Komae and Tsukuba) in the Kanto area using the simulations and the measurements. The simulations include NICAM-g6str, NICAM-g6, and the Community Multiscale Air Quality (CMAQ) driven by the Weather Research and Forecasting (WRF) model named WRF-CMAQ shown by their Figures 5 and 6 of Shimadera et al. (2013). Shimadera et al. (2013) calculated the WRF-CMAQ with a horizontal resolution of 5 km and an emission inventory that is similar to that in the present study. Table 2 summarizes the statistical parameters for the concentrations of EC, sulfate, and SO_2. The temporal variation and the average of EC simulated by NICAM-g6str are better agreement with the observations obtained for Komae than those simulated by NICAM-g6 (Figure 11(c)). However, the averages of both NICAM-g6str and NICAM-g6 simulated EC concentrations at the other sites are much underestimated compared to the observations (Table 2). For Tsukuba shown in Figure 11(d), both the NICAM-g6str and NICAM-g6 simulated EC concentrations tend to be underestimated compared with the observed concentrations, especially during the daytime, even though the temporal variation of EC obtained by NICAM-g6str is closer to the observed one compared to those obtained by NICAM-g6. At Maebashi and Kisai, the temporal variation and the averages of EC obtained by NICAM-g6 are also underestimated compared with the observations by a factor of three to five. NICAM-g6str tends to have daily maximums of EC concentrations during the morning time, whereas NICAM-g6 tends to have daily maximums during the nighttime. The temporal variations of NICAM-g6str-simulated EC concentrations are generally comparable to those by WRF-CMAQ shown in Figure 11 and their Figure 3 of Chatani et al. (2014), with the exception of the results at Maebashi and Kisai where the EC concentrations obtained by NICAM-g6str are smaller than those obtained by WRF-CMAQ. At these sties, the difference in the EC concentrations between NICAM-g6str and WRF-CMAQ is probably caused by the difference in the horizontal resolution, which is most likely critical for properly simulating the air pollution delivered by the meteorological wind fields from the center of the Kanto region (Kusaka and Hayami, 2006). Table 2 also shows that the R obtained by NICAM-g6str at all sites are high or moderate, with the exception of Maebashi, whereas those obtained by NICAM-g6 and CMAQ are low. At most sites, the EC concentrations obtained by WRF-CMAQ shown in Figure 11, and WRF-CMAQ illustrated by Morino et al. (2010a,b) and Chatani et al. (2014), NICAM-g6str, and NICAM-g6 are also underestimated compared to the observations with the larger values of RSME. The underestimation of EC concentrations is investigated by sensitivity tests of EC emission inventory in section 3.2.2.

At the same four sites, simulated sulfur components (sulfate and SO_2) are compared with the observations in Figures 12 and 13. The observed SO_2 represents the ensemble results of monitoring stations operated by Japanese and local governments around each FAMIKA site. The mean differences in the sulfate mass concentrations between NICAM-g6str and the observations are within approximately 10% at Maebashi and Tsukuba, approximately -30% at Komae, and approximately +40% at Kisai. At all sites, the temporal variations of the NICAM-g6str-simulated sulfate concentrations are generally comparable to those obtained by the observations and WRF-CMAQ shown in Figure 12 (i.e., their Figure 6 of Shimadera et al., 2013) and illustrated in their Figure 3 of Morino et al. (2010a), whereas the differences in the sulfate concentrations between NICAM-g6str and the observations are somewhat greater on August 7 and 8 at Maebashi where the performance of NICAM-g6str is relatively poor, mainly due to the inadequate horizontal resolution to reproduce the observed meteorological fields, as shown in section 3.1. The use of the prescribed distributions of three hourly averaged monthly oxidants may partly cause the discrepancy of the hourly variations of the sulfate between NICAM-g6str and the observations. The R obtained by all the models (NICAM-g6str, NICAM-g6, and WRF-CMAQ) is acceptable at most sites, with the exception of NICAM-g6str at Maebashi and WRF-CMAQ at Kisai. The RMSEs obtained by all the models are smaller at Komae and Tsukuba than those at Maebashi and Kisai. The six-hourly variations of the sulfate obtained by WRF-CMAQ are sometimes missed by NICAM-g6str, partly due to the use of the prescribed oxidants. Even though NICAM-g6 reproduces the synoptic cycle of the observed sulfate, it has difficulties in simulating the diurnal cycle of the observed and NICAM-g6str-simulated sulfate, as shown in the results of EC by Figure 11. The averages of the sulfate concentrations obtained by NICAM-g6 tend to be smaller than those by NICAM-g6str and the observations. The possible impacts of the prescribed oxidant on the sulfate concentrations are investigated in section 3.2.2.

In Figure 13, NICAM-g6str and NICAM-g6 simulated SO_2 concentrations are compared by the observations. In the previous studies, the comparison in SO_2 concentrations between the simulation and observation was very limited, with the exception of their Figure 4 of Morino et al. (2010b), which showed large differences in the SO_2 concentrations between WRF-CMAQ and the observations by more than a factor of two. The R between NICAM-g6str and the observations are low, with the exception of Komae (R=0.62), but are approximately within the range obtained by WRF-CMAQ in Morino et al. (2010b). The differences in the mean SO_2 concentrations between NICAM-g6str and the observations and between NICAM-g6 and the observations are within approximately 20% at all sites, with the exception of NICAM-g6str at Maebashi and NICAM-g6str at Tsukuba (Table 2). The temporal variations in the simulated SO_2 concur with those in the observations. The observations sometimes show high SO_2 concentrations at all sites, e.g., up to 20 ppbv at Komae, in the afternoon on August 12 and 14. On August 12, NICAM-g6str normally reproduced the peaks of the observed SO_2, but with the blunter and slightly shifted peaks. In the NICAM-g6str simulation, the strong SO_2 plumes from industrial sources over the Tokyo Bay arrived at the inner areas such as Kisai. On August 14, although the NICAM-g6str-simulated winds were comparable to the observed ones (Figures 7 and 8), NICAM-g6str did not reproduce the sharp peaks of the observed SO_2, especially at Komae and Tsukuba. It may imply that special meteorological fields cause the observed peaks on August 12, whereas unaccounted SO_2 emission from local sources or sporadic volcanoes is stronger on August 14. The latter issue is improved by processing time-highly-resolved emission inventories of SO_2, which can be estimated through a top-down approach using a data assimilation (Schutgens et al., 2012; Xu et al., 2013).

To assess the performance of both NICAM-gs6tr and NICAM-g6 in simulating the distributions of the air pollutants over Japan, we compared the August averages of the simulated EC, sulfate and SO_2 concentrations with the available measurements (Figures 14 and 15). Although the EC observatories are limited, both the NICAM-g6str and NICAM-g6 simulated EC concentrations are much underestimated compared to the observations, with the relative bias (*Br*), defined as a ratio of the simulated value to the observed one, to be 0.15 (NICAM-g6str) and 0.16 (NICAM-g6). In China, the NICAM-g6str-simulated EC concentrations are comparable to the NICAM-g6-simulated ones with the R values of 0.71 (NICAM-g6str) and 0.68 (NICAM-g6), whereas in Japan (no available measurements) the NICAM-g6str-simulated EC concentrations are larger than NICAM-g6-simulated ones at the Japanese urban areas such as Nagoya (136.97°E, 35.17°N) and Osaka (135.54°E, 34.68°N).

The NICAM-g6str-simulated sulfate concentrations are larger and more comparable to the observations over China compared to NICAM-g6-simulated ones. In Japan, the hot spots with greater concentrations of more than 5 $\mu g/m^3$ are found only in the NICAM-g6str results. The *Br* values are estimated to be 0.59 (NICAM-g6str) and 0.53 (NICAM-g6), whereas the R values are estimated to be 0.78 (NICAM-g6str) and 0.88 (NICAM-g6), respectively. The results indicate that the sulfate concentrations obtained by both NICAM-g6str and NICAM-g6 tend to be underestimated by approximately 40-50% compared with the observed sulfate concentrations. The underestimation over East Asia is mainly caused by the underestimation in China and possibly by the uncertainty of the simulated precipitation around Japan. At Hedo located at Okinawa islands, for example, the underestimation of both NICAM-g6str and NICAM-g6 simulated sulfate concentrations is caused by a possible underestimation of transboundary sulfate from the continent, which is attributed to a large uncertainty of the precipitation fields modulated by typhoon in the early August. However, the correlations of sulfate between the simulations (both NICAM-g6str and NICAM-g6) and observations are adequately acceptable. The simulated and observed SO_2 concentrations also correlate, with the R value of 0.63 (NICAM-g6str) and 0.48 (NICAM-g6). The Br values are calculated to be 0.48 (NICAM-g6str) and 0.67 (NICAM-g6). Figure 15 shows that the SO_2, which is a primary product, is localized near the source areas, whereas sulfate, which is as a secondary product, is distributed from the source to the outflow areas. Although EC is also a primary product, the horizontal distributions of NICAM-g6str-simulated EC are larger than those of NICAM-g6str-simulated SO_2, possibly because EC is less scavenged through the dry deposition and oxidation processes compared to SO_2.

3.2.2 Uncertainty in the simulation

Sensitivity tests were conducted to examine potential uncertainties derived from prescribed datasets related to EC and sulfate for the NICAM−g6str simulations. For the EC sensitivity tests, the emission quantities were set to half and twice of those used in the standard run in this study. The results for the FAMIKA sites are shown in Figure 16(a) in which the bars show the simulated EC concentrations for both sensitivity tests. For the majority of the sites, with the exception of Komae, the results obtained by the sensitivity experiments of twice strength remain underestimated compared with the measurements. The large underestimation of the EC mass concentrations at Maebashi and Kisai was also shown by WRF-CMAQ of Shimadera et al. (2013) as well as the previous studies of WRF-CMAQ in Morino et al. (2010a,b) and Chatani et al. (2014). However, Fushimi et al. (2011) and Chatani et al. (2014) suggested that the difference in the EC concentrations between WRF-CMAQ and the measurements is largely attributed to an underestimation of the EC emission inventory, especially open biomass burning from domestic sources. The local EC emission can be estimated by a combination of the data assimilation and intensive measurements (Schutgens et al., 2012; Wang et al., 2012; Yumimoto and Takemura, 2013).

Sensitivity experiments of the SO_2 emissions and the prescribed OH radical used in sulfur chemistry were executed under half and twice the amounts used in the standard experiment. The results for the FAMIKA sites are shown in Figure 16(b) in which the bars show the simulated sulfate concentrations for both sensitivity tests under the different experiments. Compared with the SO_2 emissions used in the standard experiment, the doubled amount of SO_2 emissions can overcome the slight underestimation of the simulated sulfate compared with the observations. Therefore, the emission inventories of SO_2 should be improved for the better simulation of the sulfate.

In this sensitivity tests for oxidants, the SO_2 oxidation by OH radical strongly depends on the OH concentrations as well as the cloud cover area, whereas the SO_2 oxidation by ozone and hydrogen peroxide mainly depends on their concentrations, the cloud cover area, and the cloud water content. The cloud distributions are modulated by some feedbacks of the sulfate formation through the aerosol direct and indirect effects. As a result, the sensitivity of the OH radical concentrations to the simulated sulfate concentration is smaller than that we expected and that to the SO_2 emissions. We also determined that the sensitivities of the other oxidants to the simulated sulfate concentrations were small (not shown). These results and Figures 14 and 15 also suggest that the use of the prescribed oxidants for sulfate formation is not crucial for predicting monthly- and weekly-averaged sulfate mass concentrations at least by taking into account for diurnal and seasonal variations of the prescribed oxidants. At the same time, they also suggest that because the relationship between the oxidants and the sulfate concentrations through the feedbacks is non-linear and complex, the use of the prescribed oxidants for sulfate formation can affect the hourly variations of the sulfate concentrations, and thus the sensitivity of the oxidants to the simulated sulfate should be investigated.

3.2.3 PM2.5

Figure 17 shows the temporal variation in the surface PM2.5 mass concentration at the 18 Japanese sites including 10 sites in the Kanto area using different Y-axes for the observed and simulated values. At most of the sites, both NICAM-g6str and NICAM-g6 usually captures the synoptic variation of the observed PM2.5, whereas only NICAM-g6str reproduces the diurnal variation of the observed PM2.5. Table 3 shows the PM2.5 concentrations in daily, daytime (from 9 am to 4 pm), and nighttime (from 9 pm to 4 am) averages and ratios of daytime to nighttime. The results show that the simulated PM2.5 concentrations are underestimated compared with the observations by more than a factor of two and by up to four at Maebashi. As for the diurnal variation, the results show that the NICAM-g6str-simulated ratios (0.9-1.3) are larger than NICAM-g6-simulated ones (0.8-0.9), whereas the NICAM-g6str-simulated ones are smaller than the observed values (1.0-1.8). At Maebashi, where the ratio is higher than that at other sites, the issue of the poor model performance of the meteorological fields can be a major reason of the large underestimation, as mentioned in section 3.1. At all sites, especially Maebashi and Kisai, the possible underestimation of SOA may be a critical issue, as shown in the fact that the clear diurnal variation of PM2.5 during August 4-9 and the high value of the ratios o daytime to nighttime and suggested by previous studies (Matsui et al., 2009; Morino et al., 2010c). Morino et al. (2010c) implied that over the Kanto area SOA from anthropogenic sources, which were disregarded in this study, are large portion of total carbonaceous aerosols, even though WRF-CMAQ does not correctly reproduce such carbonaceous aerosols. More sophisticated SOA module, e.g., volatility basis-set approach proposed by Donahue et al. (2006) based on the categorization of organic vapors with similar volatility, is required for to produce SOA with higher accuracy. Originally, the underestimation of PM2.5 is common among previous studies that employed regional aerosol-transport models (Morino et al., 2010b, Chatani et al., 2011), primarily because the concentrations of the observed PM2.5 include undefined chemical species with mean fractions ranging from approximately 30–50% in the total PM2.5 in the summer of Japan (datasets from the Tokyo Environment Agency and the Kawasaki Municipal Research Institute for Environmental Protection). Another possible reason is that the PM2.5 mass concentration includes water attached to aerosols, depending on the ambient RH conditions. Therefore, these undefined chemical compounds in this study may account for a large portion of the difference between the simulated and the observed values.

To evaluate the vertical profiles of the PM2.5 mass concentrations, we used the LIDAR observation operated by the NIES-Japan network. Figure 18 shows the average results for the simulated and observed extinction coefficient of the spherical particles at Tsukuba and Chiba in August. At both sites, the vertical profiles and the magnitudes below 3 km height of the simulated extinction by both NICAM-g6str and NICAM-g6 are comparable to the observed results, whereas the simulated extinction values tend to be smaller than the observed extinction values near the surface. These results near the surface are consistent with those obtained by the surface PM2.5 comparison shown in Figure 17. In contrast, the extinction values observed by LIDAR include large variabilities, primarily because they are retrieved from the surface to the cloud base, which highly varies hour-by-hour and is basically difficult to detect with the high accuracy, and secondly because they depend not only on the PM2.5 mass concentrations but also on the ambient RH and the water amount attached to aerosols. At both sites, the differences in the extinction between NICAM-g6str and NICAM-g6 are small below 1 km height, whereas those are relatively large above 1 km height. The differences are attributed to the differences in the primary particles, mainly carbonaceous aerosols, between NICAM-g6str and NICAM-g6 (not shown). It means that it is attributed to the difference in the vertical transport between different spatial resolutions. Therefore, impacts of the difference in the spatial resolution on the distributions of both aerosols and their precursors should be addressed in the future work.

4 Summary

An aerosol-coupled global nonhydrostatic model, which is based on the aerosol module of Spectral Radiation-Transport Model for Aerosol Species (SPRINTARS) and the global cloud-resolving model of Nonhydrostatic Icosahedral Atmospheric Model (NICAM), with a horizontal resolution of approximately 10 km or less in the target region, is proposed in the present study. Circulations over both the global and target domains are solved with a single model, whose mesh size varies with fine meshes covering the target region, to calculate meso-scale circulations in the study region. The stretched global model requires lower computational costs to simulate atmospheric aerosols with fine horizontal resolutions compared with the global uniform nonhydrostatic model, whereas it may require higher computational costs compared with the general regional models, because the stretched-grid system calculates inside and outside the target domain. As opposed to the general regional models, the stretched-grid system does require neither nesting techniques nor boundary conditions.

In this study, we developed the new-type regional model with a horizontal resolution of approximately 10 km to simulate aerosols over Japan, especially in the megacities of the Kanto area, including Tokyo. To evaluate the model performances in the stretched-grid system (hereafter referred to as the "NICAM-g6str"), we also simulated NICAM-SPRINTARS with the globally uniformed grid simulation in glevel-6 resolution (the horizontal resolution is set to 110 km and we call it "NICAM-g6"). Both NICAM-g6str and NICAM-g6 well reproduce general circulations obtained by reanalysis of NCEP-FNL under the nudging technique over Asia including the target region. Only NICAM-g6str usually reproduces both diurnal and synoptic variations of the observed weather (temperature, wind, and precipitation) around Japan. Both NICAM-g6str and NICAM-g6 generally reproduce monthly mean distributions of the observed sulfate and SO_2 over East Asia, with the high correlations of more than 0.5, but the underestimation of the simulated concentrations by 40% (NICAM-g6str) and 50% (NICAM-g6). The underestimation is mainly caused by the underestimation in China and possibly by the uncertainty of the simulated precipitation around Japan. In the Kanto area, the results obtained by NICAM-g6str are much closer to the observations compared to those obtained by NICAM-g6. Only NICAM-g6str succeeds in simulating the wind patterns and the diurnal transitions around the center of the Kanto area, although it is inadequate to simulate the wind patterns and the diurnal transitions at some sites located at the edge of the Kanto area and surrounded on three sides by mountains, e.g., Maebashi, mainly due to the insufficient horizontal resolution. NICAM-g6str also generally reproduces both diurnal and synoptic variations of the observed and/or a regional aerosol-transport model (WRF-CMAQ) simulated EC, sulfate, and SO_2 concentrations, especially with their high correlation ($R>0.5$) at Komae/Tokyo. The standard and sensitivity experiments suggest that (1) emission inventories of EC and SO_2 should be improved for the better simulation and (2) the use of the prescribed oxidants for the sulfate formation is not crucial for predicting weekly and monthly averaged sulfate mass concentrations at least if the diurnal and seasonal variations of the prescribed oxidants are considered. As for PM2.5 simulations, only NICAM-g6str captures both synoptic and diurnal cycles of PM2.5, with the exception of the underestimation of the simulated PM2.5 by at least twice, probably due to the underestimation of secondary organic aerosol (SOA) from anthropogenic sources and the high uncertainties of the measurements.

Therefore, this new seamless aerosol-transport model, which covers global to regional scales, can be applied to regional simulations. It suggests that even the simplified aerosol module (e.g., prescribed oxidants for sulfur chemistry) is applicable for the regional simulation if the module is coupled to a dynamic core with high horizontal resolution. To more accurately simulate areas around Japan and develop the simplified aerosol module, we need to address the following objectives: (1) to increase the horizontal resolution (less than 10 km) to properly resolve wind fields, which can greatly influence the delivery of air pollution from Tokyo to subcities such as Maebashi; (2) to accurately reproduce the cloud and precipitation fields caused by thermal lows, for example, by applying the finer horizontal resolution and/or more sophisticated schemes of cloud microphysics such as the double-moment bulk scheme proposed by Seiki and Nakajima (2014); (3) to use better emission inventories by developing a data assimilation such as the Kalman smoother proposed by Schutgens et al. (2012) with intensive measurements in many sites; (4) to simulate strong peaks of PM2.5 in the daytime in the Kanto region by implementing more sophisticated module of SOA formed from both anthropogenic and biogenic sources, such as the volatility basis-set approach proposed by Donahue et al. (2006), in this model; and (5) to treat nitrate aerosol through a thermodynamic equilibrium in the simulation of wintertime and/or future scenarios where the relative contribution of nitrate will be larger than that of sulfate under the changes in emission of NO_x and SO_2 (e.g., Ohara et al., 2007). These issues are directly connected to the further development of NICAM-SPRINTARS in both regional and global simulations. Near the future, we will present scenario experiments at regional scales of 10 km grids and/or address the issue of regional air quality and its health impacts in densely populated megacities.

Acknowledgements

We acknowledge the developers of NICAM and SPRINTARS, especially K. Suzuki and T. Takemura, and the researchers from FAMIKA, especially S. Hasegawa and Y. Morino, and Y. R. Li and A. Miyaji for their assistance with processing the datasets. We are grateful to the GTOPO30 courtesy of the U.S. Geological Survey, the NCEP-FNL, EAGrid2000 by A. Kannari, and the local government measurements provided by the Tokyo Environment Agency, the Gunma Prefectural Institute of Public Health and Environmental Sciences and the Kawasaki Municipal Research Institute for Environmental Protection. We are also grateful to the working group members of Project SALSA and the Ministry of Education, Culture, Sports and Science and Technology (MEXT). Some of the authors were supported by Project SALSA, which is part of the Research Program on Climate Change Adaptation (RECCA) by the MEXT in Japan, the Global Environment Research Fund S-12 and A-1101 of the Ministry of the Environment (MOE) in Japan, MOE/GOSAT, JST/CREST/EMS/TEEDDA, JAXA/EarthCARE, GCOM-C, MEXT/VL for climate diagnostics and

MEXT/KAKENHI/Innovative Areas 2409. The model simulations were performed using supercomputer resources, SR16000 and PRIMEHPC FX10 from the University of Tokyo, Japan.

References

Aonashi, K., Awaka, J., Hirose, M., Kozu, T., Kubota, T., Liu, G., Shige, S., Kida, S. Seto, S., Takahashi, N., and Takayabu, Y. N.: GSMaP passive, microwave precipitation retrieval algorithm: Algorithm description and validation. J. Meteor. Soc. Japan, 87A, 119-136, 2009.

Arakane, S., Satoh, M., and Yanase, W.: Excitation of deep convection to the north of tropical storm Bebinca (2006), J. Meteorol. Soc. Japan, 92(2), 141-161, doi:10.2151/jmsj.2014-201, 2014.

Arakawa, A., and Schubert, W. H.: Interactions of cumulus cloud ensemble with the large-scale environment, part I, J. Atmos. Sci., 31, 674–701, doi: 10.1175/1520-0469(1974)031<0674:IOACCE>2.0.CO;2, 1974.

Barrie, L. A., YI, Y., Leaitch, W. R., Lohmann, U., Kasibhatla, P., Roelofs, G.-J., Wilson, J., McGovern, F., Benkovitz, C., Melieres, M. A., Law, K., Prospero, J., Kritz, M., Bergmann, D., Bridgeman, C., Chin, M., Christensen, J., Easter, R., Feichter, J., Land, C., Jeuken, A., Kjellstrom, E., Koch, D., and Rasch, P.: A comparison of large-scale atmospheric sulphate aerosol models (COSAM): overview and highlights, Tellus, 53B, 615-645, 2001.

Berry, E. X.: Cloud droplet growth by collection, J. Atmos. Sci., 24, 688-701, 1967.

Chatani, S., Morikawa, T., Nakatsuka, S., and Matsunaga, S.: Sensitivity analysis of domestic emission sources and transboundary transport on PM2.5 concentrations in three major Japanese urban areas for the year 2005 with the three-dimensional aie quality simulation, J. Jpn. Soc. Atmos. Environ., 46, 101-110, 2011 (in Japanese).

Chatani, S., Morino, Y., Shimadera, H., Hayami, H., Mori, Y., Sasaki, K., Kajino, M., Yokoi, T., Morikawa, T., and Ohara, T.: Multi-model analyses of dominant factors influencing elemental carbon in Tokyo metropolitan area of Japan, Aerosol and Air Quality Research, 14, 396-405, 2014.

Chow, J. C., Watson, J. G., Crow, D., Lowenthal, D. H., and Merrifield, T.: Comparison of IMPROVE and NIOSH carbon measurements. Aerosol Sci. Technol., 34, 23–34, 2001.

Dai, T., Goto, D., Schutgens, N.A.J., Dong, X., Shi, G., and Nakajima, T.: Simulated aerosol key optical properties over global scale using an aerosol transport model coupled with a new type of dynamic core, Atmos. Environ., 82, 71-82, doi:10.1016/j.atmosenv.2013.10.018, 2014a.

Dai, T., Schutgens, N. A. J., Goto, D., Shi, G., and Nakajima, T.: Improvement of aerosol optical properties modeling over Eastern Asia with MODIS AOD assimilation in a global non-hydrostatic icosahedral aerosol transport model, Environmental Pollution, 195, 319-329, DOI: 10.1016/j.envpol.2014.06.021, 2014.

Diehl, T., Heil, A., Chin, M., Pan, X., Streets, D., Schulz, M., and Kinne, S.: Anthropogenic, biomass burning, and volcano emissions of black carbon, organic carbon, and SO_2 from 1980 to 2010 for hindcast model experiments, Atmos. Chem. Phys. Discuss., 12, 24895-24954, doi:10.5194/acpd-12-24895-2012, 2012.

Dockery, D. W., Pope III, C. A., Xu, X., Spengler, J. D., Ware, J. H., Fay, M. E., Ferris, Jr., B. G., and Speizer, F. E.: An association between air pollution and mortality in six U.S. cities, New Engl. J. Med., 329, 1753-1759, doi:10.1056/NEJM199312093292401, 1993.

Donahue, N. M., Robinson, A. L., Stanier, C. O., and Pandis, S. N.: Coupled partitioning, dilution, and chemical aging of semivolatile organics, Environ. Sci. Technol., 40, 2635-2643, 2006.

Forster, P., Ramaswamy, V., Artaxo, P., Berntsen, T., Betts, R., Fahey, D. W., Haywood, J., Lean, J., Lowe, D. C., Myhre, G., Nganga, J., Prinn, R., Raga, G., Schulz, M., and Van Dorland, R.: Changes in Atmospheric Constituents and in Radiative Forcing. In: Climate Change 2007: The Physical Science Basis. Contribution of Working Group I to the Fourth Assessment Report of the Intergovernmental Panel on Climate Change, edited by: Solomon, S., Qin, D., Manning, M., Chen, Z., Marquis, M., Averyt, K. B., Tignor, M., and Miller, H. L., Cambridge University Press, Cambridge, United Kingdom and New York, NY, USA, 996pp., 2007.

Fushimi, A., Wagai, R., Uchida, M., Hasegawa, S., Takahashi, K., Kondo, M., Hirabayashi, M., Morino, Y., Shibata, Y., Ohara, T., Kobayashi, S., and Tanabe, K.: Radiocarbon (^{14}C) diurnal variations in fine particles at sites downwind from Tokyo, Japan in summer, Environ. Sci. Technol., 45, 6784-6792, doi:10.1021/es201400p, 2011.

Goto, D., Nakajima, T., Takemura, T., and Sudo, K.: A study of uncertainties in the sulfate distribution and its radiative forcing associated with sulfur chemistry in a global aerosol model, Atmos. Chem. Phys., 11, 10889-10910, doi:10.5194/acp-11-10889-2011, 2011a.

Goto, D., Schutgens, N. A. J., Nakajima, T., and Takemura, T.: Sensitivity of aerosol to assumed optical properties over Asia using a global aerosol model and AERONET, Geophys. Res. Lett., 38, doi:10.1029/2011GL048675, 2011b.

Goto, D., Takemura, T., Nakajima, T., and Badarinath, K. V. S.: Global aerosol model-derived black carbon concentration and single scattering albedo over Indian region and its comparison with ground observations, Atmos. Environ., 45, 3277-3285, doi:10.1016/j.atmosenv.2011.03.037, 2011c.

Goto, D.: Modeling of black carbon in Asia using a global-to-regional seamless aerosol-transport model, Environmental Pollution, 195, 330-335, DOI: 10.1016/j.envpol.2014.06.006, 2014.

Hallquist, M., Wenger, J. C., Baltensperger, U., Rudich, Y., Simp- son, D., Claeys, M., Dommen, J., Donahue, N. M., George, C., Goldstein, A. H., Hamilton, J. F., Herrmann, H., Hoff- mann, T., Iinuma, Y., Jang, M., Jenkin, M. E., Jimenez, J. L., Kiendler-Scharr, A., Maenhaut, W., McFiggans, G., Mentel, Th. F., Monod, A., Prevot, A. S. H., Seinfeld, J. H., Surratt, J. D., Szmigielski, R., and Wildt, J.: The formation, properties and im- pact of secondary organic aerosol: current and emerging issues, Atmos. Chem. Phys., 9, 5155–5236, doi:10.5194/acp-9-5155-2009, 2009.

Hasegawa, S., Kobayashi, S., Ohara, T., Tanabe, K., Hayami, H., Yomemochi, S., Umezawa, N., Iijima, A. and Kumagai, K.: Fine aerosol measurement and modeling in Kanto area (1), overview of measurement. Proceedings of the 49th Annual Meeting of the Japan Society for Atmospheric Environment, 377, 2008 (in

Japanese).

Holloway, T., Sakurai, T., Han, Z., Ehlers, S., Spak, S.N., Horowitz, L. W., Carmichael, G. R., Streets, D. G., Hozumi, Y., Ueda, H., Park, S. U., Fung, C., Kajino, M., Thongboonchoo, N., Engardt, M., Bennet, C., Hayami, H., Sartelet, K., Wang, Z., Matsuda, K., and Amann, M.: MICS-Asia II: Impact of global emissions on regional aiq quality in Asia, Atmos. Environ., 42, 3543-3561, 2008.

Kannari, A., Tonooka, Y. Baba, T., and Murano, K.: Development of multiple-species 1 km x 1 km resolution hourly basis emissions inventory for Japan, Atmos. Environ., 41, 3428-3439, 2007.

Kawabata, T., Kuroda, T., Seko, H., and Saito, K.: A Cloud-Resolving 4DVAR Assimilation Experiment for a Local Heavy Rainfall Event in the Tokyo Metropolitan Area. Mon. Wea. Rev., 139, 1911–1931, 2011.

Kinne, S., Schulz, M., Textor, C., Guibert, S., Balkanski, Y., Bauer, S. E., Berntsen, T., Boucher, O., Chin, M., Collins, W., Dentener, F., Diehl, T., Easter, R., Feichter, J., Fillmore, D., Ghan, S., Ginoux, P., Gong, S., Grini, A., Hendricks, J., Herzog, M., Horowitz, L., Isaksen, I., Iversen, T., Kirkevag, A., Kloster, S., Koch, D., Kristjansson, J. E., Krol. M., Lauer, A., Lamarque, J. F., Lesins, G., Liu, X., Lohmann, U., Montanaro, V., Myhre, G., Penner, J. E., Pitari, G., Reddy, S., Seland, O., Stier, P., Takemura, T., and Tie, X.: An AeroCom initial assessment – optical properties in aerosol component modules of global models, Atmos. Chem. Phys., 6, 1815-1834, doi:10.5194/acp-6-1815-2006, 2006.

Kitada, T., Okamura, K., and Tanaka, S.: Effects of topography and urbanization on local winds and thermal environment in the Nohbi Plain, coastal region of central Japan: A numerical analysis by mesoscale meteorological model with a k-e turbulence model, J. Applied Met., 37, 1026-1046, 1998.

Kubota, T., Shige, S., Hashizume, H., Aonashi, K., Takahashi, N., Seto, S., Hirose, M., Takayabu, Y. N., Nakagawa, K., Iwanami, K., Ushio, T., Kachi, M., and Okamoto, K.: Global Precipitation Map using Satelliteborne Microwave Radiometers by the GSMaP Project: Production and Validation, IEEE Trans. Geosci. Remote Sens., 45(7), 2259-2275, 2007.

Kurokawa, J., Ohara, T., Morikawa, T., Hanayama, S., Greet, J.-M., Fukui, T., Kawashima, K., and Akimoto, H.: Emissions of air pollutants and greenhouse gases over Asian regions during 2000-2008: Regional emission inventory in Asia (REAS) version 2, Atmos. Chem. Phys. Discuss., 13, 10049-10123, 2013.

Kusaka, H., and Hayami, H.: Numerical simulation of local weather for a high photochemical oxidant event using the WRF model, JSME International Journal. Ser. B. Fluids and thermal engineering, 49(1), 72-77, 2006.

Kuwagata, T., and Sumioka, M.: The daytime PBL heating process over complex terrain in central Japan under fair and calm weather conditions, Part III: Daytime thermal low and nocturnal thermal high, J. Met. Soc. Japan, 69(1), 91-104, 1991

Le Treut, H., and Li, Z.-X.: Sensitivity of an atmospheric general circulation model to prescribed SST changes: feedback effects associated with the simulation of cloud optical properties, Clim. Dynam., 5, 175–187, 1991.

Matsui, H., Koike, M., Takegawa, N., Kondo, Y., Griffin, R. J., Miyazaki, Y., Yokouchi, Y., and Ohara, T.: Secondary organic aerosol formation in urban air: Temporal variations and possible contributions from unidentified hydrocarbons, J. Geophys. Res., 114, D04201, doi:10.1029/2008JD010164, 2009.

Mellor, G. L. and Yamada, T.: A hierarchy of turbulence closure models for planetary boundary layers, J. Atmos. Sci., 31, 1791-1806, doi:10.1175/1520-0469(1974)031<1791:AHOTCM>2.0.CO;2, 1974.

Miura, H., Satoh, M., Nasuno, T., Noda, A. T., and Oouchi, K.: A Madden-Julian Oscillation event realistically simulated by a global cloud-resolving model, Science, 318, 1763-1765, doi:10.1126/science.1148443, 2007.

Morino, Y., Chatani, S., Hayami, H., Sasaki, K., Mori, Y., Morikawa, T., Ohara, T., Hasegawa, S., and Kobayashi, S.: Evaluation of ensemble approach for O3 and PM2.5 simulation, Asian Journal of Atmospheric Environment, 4, 150-156, 2010a.

Morino, Y., Chatani, S., Hayami, H., Sasaki, K., Mori, Y., Morikawa, T., Ohara, T., Hasegawa, S., and Kobayashi, S.: Inter-comparison of chemical transport models and evaluation of model performance for O_3 and PM2.5 prediction – case study in the Kanto Area in summer 2007, J. Jpn. Soc. Atmos. Environ., 45, 212-226, 2010b (in Japanese).

Morino, Y., Takahashi, K., Fushimi, A., Tanabe, K., Ohara, T., Hasegawa, S., Uchida, M., Takami, A., Yokouchi, Y., and Kobayashi, S.: Contrasting diurnal variations in fosil and nonfossil secondary organic aerosols in urban outflow, Japan, Environ. Sci. Technol., 44, 8581-8586, 2010c.

Nakajima, T., Tsukamoto, M., Tsushima, Y., Numaguti, A., and Kimura, T.: Modeling of the radiative process in an atmospheric general circulation model, Appl. Optics, 39, 4869–4878, doi:10.1364/AO.39.004869, 2000.

Nakanishi, M. and Niino, H.: An improved Mellor–Yamada level 3 model with condensation physics: Its design and verification, Bound.-Lay. Meteorol., 112, 1-31, doi:10.1023/B:BOUN.0000020164.04146.98, 2004.

Nakanishi, M. and Niino, H.: Development of an improved turbulence closure model for the atmospheric boundary layer, J. Meteorol. Soc. Japan, 87, 895-912, doi:10.2151/jmsj.87.895, 2009.

Nasuno, T.: Forecast skill of Madden-Julian Oscillation events in a global nonhydrostatic model during the CINDY2011/DYNAMO observation period, SOLA, 9, 69-73, doi:10.2151/sola.2013-016, 2013.

Niwa, Y., Tomita, H., Satoh, M., and Imasu, R.: A three-dimensional icosahedral grid advection scheme preserving monotonicity and consistency with continuity for atmospheric tracer transport, J. Meteorol. Soc. Jpn., 89, 255-268, doi:10.2151/jmsj.2011-306, 2011.

Noda, A. T., Oouchi, K., Satoh, M., Tomita, H., Iga, S., and Tsushima, Y.: Importance of the subgrid-scale turbulent moist process of the turbulent transport: On cloud distribution in global cloud-resolving simulations, Atmos. Res., 96, 208-217, doi:10.1016/j.atmosres.2009.05.007, 2009.

Ohara, T., Akimoto, H., Kurokawa, J., Horii, N., Yamaji, K., Yan, X., and Hayasaka, T.: An Asian emission inventory of anthropogenic emission sources for the perid 1980-2020, Atmos. Chem. Phys., 7, 4419-4444, 2007.

Okamoto, K., Iguchi, T., Takahashi, N., Iwanami, K., and Ushio, T.: The global satellite mapping of precipitation (GSMaP) project, 25th IGARSS Proceedings, 3414-3416, 2005.

Pope III, C. A., Ezzati, M., and Dockery, D. W.: Fine-particulate air pollution and life expectancy in the United States, N. Engl. J. Med., 360, 376-386, doi:10.1056/NEJMsa0805646, 2009.

Ramanathan, V., Akimoto, H., Bonasoni, P., Brauer, M., Carmichael, G., Chung, C. E., Feng, Y., Fuzzi, S., Hasnain, S. I., Iyngararasan, M., Jayaraman, A., Lawrence, M. G., Nakajima, T., Panwar, T. S., Ramana, M. V., Rupakheti, M., Weidemann, S., and Yoon, S.-C.: Atmosphere brown clouds and regional climate change, part I of atmosphere brown clouds: Regional assessment report with focus on Asia, Project Atmosphere Brown Cloud, United National Environment Programme, Nairobi, Kenya, 2008.

Randall, D. A., Heikes, R., and Ringler, T.: Global atmospheric modeling using a geodesic grid with an isentropic vertical coordinate, in: General Circulation Model Development, Academic Press, San Diego, CA, 509-538, 2000.

Saito, K., Fujita, T., Yamada, Y., Ishida, J., Kumagai, Y., Aranami, K., Ohmori, S., Nagasawa, R., Kumagai, S., Muroi, C., Kato, T., Eito, H., and Yamazaki, Y.: The Operational JMA Nonhydrostatic Mesoscale Model, Mon. Wea. Rev., 134, 1266-1298, doi: hyyp://dx.doi.org/10.1175/MWR3120.1, 2006.

Sato, T., Miura, H., Satoh, M., Takayabu, Y. N., and Wang, Y.: Diurnal cycle of precipitation in the tropics simulated in a global cloud-resolving model, J. Climate, 22, 4809-4826; doi:10.1175/2009JCLI2890.1, 2009.

Satoh, M., Matsuno, T., Tomita, H., Miura, H., Nasuno, T., and Iga, S.: Nonhydrostatic Icosahedral Atmospheric Model (NICAM) for global cloud resolving simulations, J. Comput. Phys., 227, 3486-3514, doi:10.1016/j.jcp.2007.02.006, 2008.

Satoh, M., Inoue, T., and Miura, H: Evaluations of cloud properties of global and local cloud system resolving models using CALIPSO and CloudSat simulators, J. Geophys. Res., 115, D00H14, doi:10.1029/2009JD012247, 2010.

Satoh, M., Tomita, H., Yashiro, H., Miura, H., Kodama, C., Seiki, T., Noda, A., Yamada, T., Goto, D., Sawada, M., Miyoshi, T., Niwa, Y., Hara, M., Ohno, T., Iga, S., Arakawa, T., Inoue, T., and Kubokawa, H.: The Non-hydrostatic icosahedral atmospheric model: description and development, Progress in Earth and Planetary Science, 1, 18-49, doi:10.1186/s40645-014-0018-1, 2014.

Schutgens, N., Nakata, M., and Nakajima, T.: Estimating aerosol emissions by assimilating remote sensing observations into a global transport model, Remote Sens., 4, 3528-3542, doi:10.3390/rs4113528, 2012.

Seiki, T. and Nakajima, T.: Aerosol effects of the condensation process on a convective cloud simulation, J. Atmos. Sci., 71, 833-853, doi:10.1175/JAS-D-12-0195.1, 2014.

Sekiguchi, M. and Nakajima, T.: A *k*-distribution-based radiation code and its computational optimization for an atmospheric general circulation model, J. Quant. Spectrosc. RA, 109, 2779-2793, doi:10.1016/j.jqsrt.2008.07.013, 2008.

Shimadera, H., Hayami, H., Morino, Y., Ohara, T., Chatani, S., Hasegawa, S., and

Kaneyasu, N.: Analysis of summertime atmospheric transport of fine particulate matter in northeast Asia, Asia-Pac. J. Atmos. Sci., 49, 347-360, doi:10.1007/s13143-013-0033-y, 2013.

Shimizu, A., Sugimoto, N., Matsui, I., Arao, K., Uno, I., Murayama, T., Kagawa, N., Aoki, K., Uchiyama, A., and Yamazaki, A.: Continuous observations of Asian dust and other aerosols by polarization lidars in China and Japan during ACE-Asia, J. Geophys. Res., 109, D19S17, doi: 10.1029/2002JD003253, 2004.

Stuhne, G. R. and Peltier, W. R.: Vortex erosion and amalgamation in a new model of large scale flow on the sphere, J. Comput. Phys. 128, 58-81, doi:10.1006/jcph.1996.0196, 1996.

Sudo, K., Takahashi, M., Kurokawa, J., and Akimoto, H.: CHASER: A global chemical model of the troposphere: 1. Model description, J. Geophys. Res., 107, 4339, doi:10.1029/2001JD001113, 2002.

Sugimoto, N., Uno, I., Nishikawa, M., Shimizu, A., Matsui, I., Dong, X., Chen, Y., Quan, H.: Record Heavy Asian Dust in Beijing in 2002: Observations and Model Analysis of Recent Events, Geophys. Res. Lett. 30(12), 1640, doi:10.1029/2002GL016349, 2003.

Suzuki, K., Nakajima, T., Satoh, M., Tomita, H., Takemura, T., Nakajima, T. Y., and Stephens, G. L.: Global cloud-system-resolving simulation of aerosol effect on warm clouds, Geophys. Res. Lett., 35, L19817, doi:10.1029/2008GL035449, 2008.

Takemura, T.: Distributions and climate effects of atmospheric aerosols from the preindustrial era to 2100 along Representative Concentration Pathway (RCPs) simulated using the global aerosol model SPRINTARS, Atmos. Chem. Phys., 12, 11555-11572, doi:10.5194/acp-12-11555-2012, 2012.

Takemura, T., Okamoto, H., Maruyama, Y., Numaguti, A., Higurashi, A., and Nakajima, T.: Global three-dimensional simulation of aerosol optical thickness distribution of various origins, J. Geophys. Res., 105, 17853-17873, doi:10.1029/2000JD900265, 2000.

Takemura, T., Nakajima, T., Dubovik, O., Holben, B. N., and Kinne, S.: Single scattering albedo and radiative forcing of various aerosol species with a global three-dimensional model, J. Climate, 15, 333-352, doi:10.1175/1520-0442(2002)015<0333:SSAARF>2.0.CO;2, 2002.

Takemura, T., Nozawa, T., Emori, S., Nakajima, T. Y., and Nakajima, T.: Simulation of climate response to aerosol direct and indirect effects with aerosol transport-radiation model, J. Geophys. Res., 110, D02202, doi:10.1029/2004JD005029, 2005.

Taylor, M., Tribbia, J., and Iskandarani, M.: The spectral element method for the shallow water equations on the sphere, J. Comput. Phys. 130, 92-108, doi:10.1006/jcph.1996.5554,1997.

Textor, C. Schulz, M., Guibert, S., Kinne, S., Balkanski, Y., Bauer, S., Berntsen, T., Berglen, T., Boucher, O., Chin, M., Dentener, F., Diehl, T., Easter, R., Feichter, J., Fillmore, D., Ghan, S., Ginoux, P., Gong, S., Grini, A., Hendricks, J., Horowitz, L., Huang, P., Isaksen, I., Iversen, T., Kloster, S., Koch, D., Kirkevåg, A., Kristjansson, J. E., Krol, M., Lauer, A., Lamarque, J. F., Liu, X., Montanaro, V., Myhre, G., Penner, J. E., Pitari, G., Reddy, S., Seland, Ø., Stier, P., Takemura, T., and Tie, X.: Analysis and quantification of the diversities of aerosol life cycles within AeroCom, Atmos. Chem. Phys., 6, 1777-1813, doi:10.5194/acp-6-1777-2006, 2006.

Turpin, B. J., and Lim, H.-J.: Species contributions to PM2.5 mass concentrations: revisiting common assumptions for estimating organic mass, Aerosol Sci. Tech., 35, 602-610, doi: 10.1080/02786820119445, 2001.

Tomita, H.: A stretched grid on a sphere by new grid transformation, J. Meteorol. Soc. Jpn., 86A, 107-119, 2008a.

Tomita, H.: New microphysics with five and six categories with diagnostic generation of cloud ice, J. Meteorol. Soc. Jpn., 86A, 121-142, 2008b.

Tomita, H. and Satoh, M.: A new dynamical framework of nonhy- drostatic global model using the icosahedral grid, Fluid Dyn. Res., 34, 357-400, 2004.

Tomita, H., Miura, H., Iga, S., Nasuno, T., and Satoh, M.: A global cloud-resolving simulation: Preliminary results from an aqua planet experiment, Geophys. Res. Lett., 32, L08805, doi:10.1029/2005GL022459, 2005.

Tomita, H., K. Goto, and Satoh, M.: A new approach of atmospheric general circulation model: Global cloud resolving model NICAM and its computational performance, SIAM J. Sci. Stat. Comp., 30, 2755-2776, doi:10.1137/070692273, 2008.

UNEP and WMO: Integrated assessment of black carbon and tropospheric ozone, United Nations Environment Programme (UNEP) and World Meteorological Organization (WMO), Nairobi, Kenya, 2011.

Ushio, T., Kubota, T., Shige, S., Okamoto, K., Aonashi, K., Inoue, T., Takahashi, N., Iguchi, T., Kachi, M., Oki, R., Morimoto, T., and Kawasaki, Z.: A Kalman filter approach to the Global Satellite Mapping of Precipitation (GSMaP) from combined passive microwave and infrared radiometric data. J. Meteor. Soc. Japan, 87A, 137-151, 2009.

Wang, J., Xum X. Q., Henze, D. K., Zeng, J., Ji, Q., Tsay, S.-C., and Huang, J. P.: Top-down estimate of dust emissions through integration of MODIS and MISR aerosol retrievals with the GEOS-Chem adjoint model, Geophys. Res. Lett., 39(8), DOI: 10.1029/2012GL051136, 2012.

Xu, X. Q., Wang, J., Henze, D. K., Qu, W. J., and Kopacz, M.: Constraints on aerosol source using GEOS-Chem adjoint and MODIS radiances, and evaluation with multisensor (OMI, MISR) data J. Geophys. Res. Atmos., 118 (12), 6396-6413, DOI: 10.1002/jgrd.50515, 2013.

Yu, H., Remer, L. A., Chin, M., Bian, H., Tan, Q., Yuan, T., and Zhang, Y.: Aerosols from overseas rival domestic emissions over North America, Science, 337, 566-569, doi:10.1126/science.1217576, 2012.

Yumimoto, K. and Takemura T.: The SPRINTARS/4D-Var Data Assimilation System: Development and Inversion Experiments Based on the Observing System Simulation Experiment Framework, Geosci. Model Dev., 6, 2005-2022, doi:10.5194/gmd-6-2005-2013, 2013.

Zhang, Q., Jimenez, J. L., Canagaratna, M. R., Allan, J. D., Coe, H., Ulbrich, I., Alfarra, M. R., Takami, A., Middlebrook, A. M., Sun, Y. L., Dzepina, K., Dunlea, E., Docherty, K., DeCarlo, P. F., Salcedo, D., Onasch, T., Jayne, J. T., Miyoshi, T., Shimono, A., Hatakeyama, S., Takegawa N., Kondo, Y., Schneider, J., Drewnick, F., Borrmann, S., Weimer, S., Demerjian, K., Williams, P., Bower, K., Bahreini, R., Cottrell, L., Griffin, R. J., Rautiainen, J., Sun, J. Y., Zhang, Y. M., and Worsnop, D. R.: Ubiquity and dominance of oxygenated species in organic aerosols in anthropogenically-influenced Northern Hemisphere midlatitudes, Geophy. Res. Lett., 34, L13801, doi:10.1029/2007GL029979, 2007.

Zhang, X. Y., Wang, Y. Q., Niu, T., Zhang, X. C., Gong, S. L., Zhang, Y. M., and Sun, J. Y.: Atmospheric aerosol compositions in China: spatial/temporal variability, chemical signature, regional haze distribution and comparisons with global aerosols, Atmos. Chem. Phys., 12, 779-799, doi: 10.5194/acp-12-779-2012, 2012.

Table 1. Statistical values (averages of the observation and simulations, correlation coefficient *R* and root-mean-square-error *RMSE*) for meteorological fields using the simulations (NICAM-g6str and NICAM-g6) and observations at seven sites during the same period, as shown in Figures 4 to 7.

		Yokohama	Chiba	Tsuchiura	Adachi	Maebashi	Machida	Kisai
		Temperature						
Average [°C] and difference [°C] (vs. observation) in bracket	Observation	27.9	30.1	28.1	29.7	29.1	29.1	27.9
	NICAM-g6str	26.9 (-1.1)	28.3 (-1.8)	28.3 (0.2)	27.3 (-2.3)	25.5 (-3.6)	25.9 (-3.2)	25.8 (-2.2)
	NICAM-g6	25.5 (-2.4)	26.2 (-3.9)	25.7 (-2.4)	25.5 (-4.1)	23.9 (-5.2)	25.5 (-3.6)	23.9 (-4.0)
R	NICAM-g6str	0.74	0.85	0.84	0.81	0.79	0.74	0.80
	NICAM-g6	0.76	0.67	0.79	0.78	0.71	0.77	0.75
RMSE [°C]	NICAM-g6str	1.9	2.3	1.9	3.0	4.3	3.9	3.0
	NICAM-g6	2.8	4.4	3.1	4.6	5.8	4.0	4.6
		RH						
Average [%] and difference [%] (vs. observation) in bracket	Observation	73.5	79.0	73.3	75.4	73.7	75.9	71.4
	NICAM-g6str	83.6 (10.0)	77.5 (-1.5)	76.4 (3.0)	77.9 (2.5)	82.7 (9.0)	82.5 (6.6)	81.6 (10.1)
	NICAM-g6	92.2 (18.6)	92.4 (13.4)	93.4 (20.0)	92.2 (16.8)	95.5 (21.9)	92.2 (16.3)	95.5 (24.1)
R	NICAM-g6str	0.64	0.68	0.69	0.72	0.72	0.72	0.81
	NICAM-g6	0.73	0.59	0.79	0.82	0.71	0.74	0.76
RMSE [%]	NICAM-g6str	12.7	8.9	11.0	10.1	14.6	12.9	13.3
	NICAM-g6	19.5	16.2	22.4	19.8	25.5	20.1	26.3
		Wind speed						
Average [m/s] and	Observation	2.9	2.6	1.6	2.6	1.2	2.7	1.9
	NICAM-g6str	4.2	3.8	3.1	3.4	3.1	3.0	2.7

difference		(1.3)	(1.1)	(1.4)	(0.9)	(1.9)	(0.3)	(0.8)
[m/s] (vs. observation) in bracket	NICAM-g6	3.7 (0.7)	5.0 (2.4)	1.0 (-0.7)	3.7 (1.1)	0.9 (-0.4)	3.7 (1.0)	0.9 (-1.0)
R	NICAM-g6str	0.72	0.41	0.65	0.51	0.19	0.59	0.16
	NICAM-g6	0.64	0.43	0.38	0.47	0.12	0.53	0.04
RMSE	NICAM-g6str	1.9	2.0	1.8	1.7	2.3	1.3	1.7
[m/s]	NICAM-g6	1.4	3.0	1.2	1.7	0.7	1.7	1.4

Table 2. Statistical values (averages of the observation and simulations, correlation coefficient *R* and root-mean-square-error *RMSE*) for EC, sulfate, and SO_2 concentrations by the simulations (NICAM-g6str, NICAM-g6, and WRF-CMAQ) and the observations at four FAMIKA sites during the period from August 6 to 11. The WRF-CMAQ results are given by Shimadera et al. (2013).

		Maebashi	Kisai	Komae	Tsukuba
		EC			
Average [μg/m^3] and difference [%] (vs. observation) in bracket	Observation	2.85	2.75	1.23	2.20
	NICAM-g6str	0.39 (-86)	0.60 (-78)	1.10 (-10)	0.73 (-67)
	NICAM-g6	0.52 (-82)	0.52 (-81)	0.49 (-60)	0.58 (-74)
	WRF-CMAQ	0.87 (-69)	1.17 (-58)	0.92 (-25)	0.77 (-65)
R	NICAM-g6str	-0.02	0.41	0.55	0.59
	NICAM-g6	-0.49	-0.28	-0.05	0.16
	WRF-CMAQ	0.08	0.33	0.37	-0.23
RMSE [μg/m^3]	NICAM-g6str	2.62	2.33	0.72	1.85
	NICAM-g6	2.52	2.45	1.10	2.06
	WRF-CMAQ	2.18	1.83	0.88	1.98
		Sulfate			
Average [μg/m^3] and difference [%] (vs. observation) in bracket	Observation	4.79 (-6)	2.86 (44)	4.18 (-32)	4.85 (-12)
	NICAM-g6str	4.51 (-34)	4.14 (11)	2.84 (-46)	4.25 (-26)
	NICAM-g6	3.17 (-21%)	3.17 (42%)	2.25 (-21%)	3.58 (-22%)
	WRF-CMAQ	3.77	4.08	3.30	3.80

R	NICAM-g6str	0.01	0.50	0.51	0.73
	NICAM-g6	0.05	0.56	0.86	0.75
	WRF-CMAQ	0.41	0.02	0.87	0.78
RMSE [μg/m^3]	NICAM-g6str	3.61	2.81	2.71	2.49
	NICAM-g6	3.01	2.30	2.49	2.77
	WRF-CMAQ	2.30	3.37	1.62	2.56
		SO_2			
Average [ppbv] and difference [%] (vs. observation) in bracket	Observation	2.74	2.28	2.35	3.79
	NICAM-g6str	1.25 (-54)	1.90 (-17)	2.34 (-1)	2.34 (-38)
	NICAM-g6	2.42 (-12)	2.45 (7)	2.52 (7)	3.21 (-15)
R	NICAM-g6str	0.02	-0.04	0.62	0.21
	NICAM-g6	-0.64	-0.52	0.22	-0.04
RMSE [ppbv]	NICAM-g6str	1.82	0.93	0.97	2.08
	NICAM-g6	1.29	0.94	0.85	1.29

Table 3. PM2.5 concentrations in daily, daytime (from 9 am to 4 pm), and nighttime (from 9 pm to 4 am) averages and mean ratios of daytime to nighttime using the simulations (NICAM-g6str and NICAM-g6) and the observation at selected seven sites in August.

	Maebashi	Kawasaki	Toride	Hasuda	Sapporo	Nagoya	Fukuoka
	Daily mean PM2.5 [μg/m^3] and standard deviation [μg/m^3]						
Observation	24.9±12.8	23.2±12.9	17.6±9.7	20.6±11.5	12.7±6.3	17.3±10.1	14.3±7.5
NICAM-g6str	6.4±3.9	10.0±7.3	9.0±6.3	8.4±5.0	4.9±3.5	7.5±5.7	3.4±2.6
NICAM-g6	6.7±3.0	6.7±3.3	6.7±3.4	6.7±3.0	4.7±4.1	5.4±3.0	3.5±2.3
	Daytime (9am-4pm) mean PM2.5 [μg/m^3] and standard deviation [μg/m^3]						
Observation	28.6±14.1	19.4±12.1	15.8±9.0	21.0±10.0	15.0±5.2	11.3±5.4	9.7±5.7
NICAM-g6str	5.9±3.8	7.1±4.3	6.8±4.4	7.2±4.5	5.3±2.8	3.5±2.3	1.6±0.8
NICAM-g6	5.0±1.7	4.0±2.1	4.0±2.4	4.4±1.9	7.4±4.5	2.4±0.9	1.4±0.5
	Nighttime (9pm-4am) mean PM2.5 [μg/m^3] and standard deviation [μg/m^3]						
Observation	24.4±11.9	24.5±11.8	16.9±9.6	18.5±10.3	10.7±6.6	19.1±8.2	15.4±6.7
NICAM-g6str	7.5±3.6	14.2±9.2	12.1±7.6	10.8±5.5	4.1±3.9	12.0±4.6	5.1±3.1

NICAM-g6	7.5±2.3	9.1±1.5	8.8±2.1	8.4±3.0	2.6±3.1	7.8±1.3	4.4±2.2
	Ratio of daytime-mean PM2.5 to nighttime-mean PM2.5						
Observation	1.8±0.8	1.7±0.5	1.3±0.4	1.2±0.4	1.0±0.4	1.3±0.4	1.1±0.3
NICAM-g6str	1.1±0.6	1.3±0.7	1.1±0.6	1.1±0.5	0.9±0.3	1.2±0.9	1.0±0.6
NICAM-g6	0.9±0.2	0.8±0.1	0.8±0.1	0.8±0.1	0.8±0.2	0.9±0.2	0.8±0.2

Figure captions

Figure 1 Topographical maps of (a) East Asia and (b) Eastern Japan, including the observation sites for the model validation. The topography is based on GTOPO30 (the horizontal resolution is 30 arc seconds, that is approximately 1 km) courtesy of the U.S. Geological Survey.

Figure 2 (a) EC and (b) SO_2 emission inventories in 2007.

Figure 3 Horizontal distributions of temperature and winds in August averages at the surface and the model height of approximately 5 km over Asia region using reanalysis data from NCEP-FNL, simulation by NICAM-g6str, and simulation by NICAM-g6.

Figure 4 Temporal variations in the NICAM-g6str and NICAM-g6 simulated and observed air temperature for a height of 2 m at (a) Yokohama, (b) Chiba, (c) Tsuchiura, (d) Adachi, (e) Maebashi, (f) Machida and (g) Kisai in August 2007.

Figure 5 Same as Figure 4 but for relative humidity (RH).

Figure 6 Same as Figure 4 but for wind direction.

Figure 7 Same as Figure 4 but for wind speed.

Figure 8 Horizontal distributions of precipitation in August averages derived from (a) simulation by NICAM-g6str, (b) simulation by NICAM-g6, (c) reanalysis data from MSM by JMA and (d) reanalysis data from GSMaP.

Figure 9 Temporal variations in the NICAM-g6str and NICAM-g6 simulated and observed precipitation amounts at 21 Japanese sites in August 2007. The comparison includes 10 sites in the Kanto area; (a) Maebashi, (b) Konosu, (c) Huchu, (d) Tsukuba, (e) Tokyo, (f) Yokohama, (g) Abiko, (h) Saitama, (i) Chiba, and (j) Nerima, 3 sites in the northern Japan; (k) Niigata, (l) Sendai, and (m) Sapporo, 5 sites in the western Japan; (n) Nagoya, (o) Osaka, (p) Himeji, (q) Fukuoka, and (r) Hyuga, and 3 remote islands (s) Hachijo-jima, (t) Oshima, and (u) Naha.

Figure 10 Predictive values of daily precipitation using the NICAM-g6str and NICAM-g6 simulations and the AMeDAS measurements during August 2007 at the sites defined at Figure 9, in units of percentage.

Figure 11 Temporal variations in the simulated (NICAM-g6str, NICAM-g6, and WRF-CMAQ) and observed EC mass concentrations near the surface at (a) Maebashi, (b) Kisai, (c) Komae and (d) Tsukuba in August 2007. The WRF-CMAQ results are given by Shimadera et al. (2013). The left axis in red represents the simulated values, and the right axis in black represents the observed values, in units of $\mu g/m^3$.

Figure 12 Same as Figure 11 but for sulfate.

Figure 13 Same as Figure 12 but for SO_2 without the WRF-CMAQ results, in units of ppbv.

Figure 14 Scatterplot of August mean concentrations for EC, sulfate and SO_2 between the simulations by NICAM-g6str and NICAM-g6 and the observations at the sites shown in the left panels. The statistics parameters, relative bias (Br) and correlation coefficient (R), calculated by the simulated and observed concentrations at all the sites, are also shown in each panel.

Figure 15 Horizontal distributions of concentrations for EC, sulfate and SO_2 near the surface using NICAM-g6str and NICAM-g6 in August averages. The circles in color shows the observation results at the sites.

Figure 16 (a) EC and (b) sulfate mass concentrations at the FAMIKA four sites using NICAM-g6str under the sensitivity experiments, WRF-CMAQ results shown by Shimadera et al. (2013) and the FAMIKA observations in averages of August 6-11. The bar represents the range of the sensitivity.

Figure 17 Temporal variations in the NICAM-g6str and NICAM-g6 simulated and observed PM2.5 near the surface at 18 Japanese sites in August 2007. The left axis in red represents the simulated values, and the right axis in black represents the observed values, in unit of μgm^{-3}.

Figure 18 Extinction coefficients in August averages for the spherical particles simulated by NICAM-g6str and NICAM-g6 and the spherical particles observed by the NIES-LIDAR network at (a) Tsukuba and (b) Chiba, in units of 1/(Mm). The bars represent the 25th and 75th percentiles of the LIDAR observations.

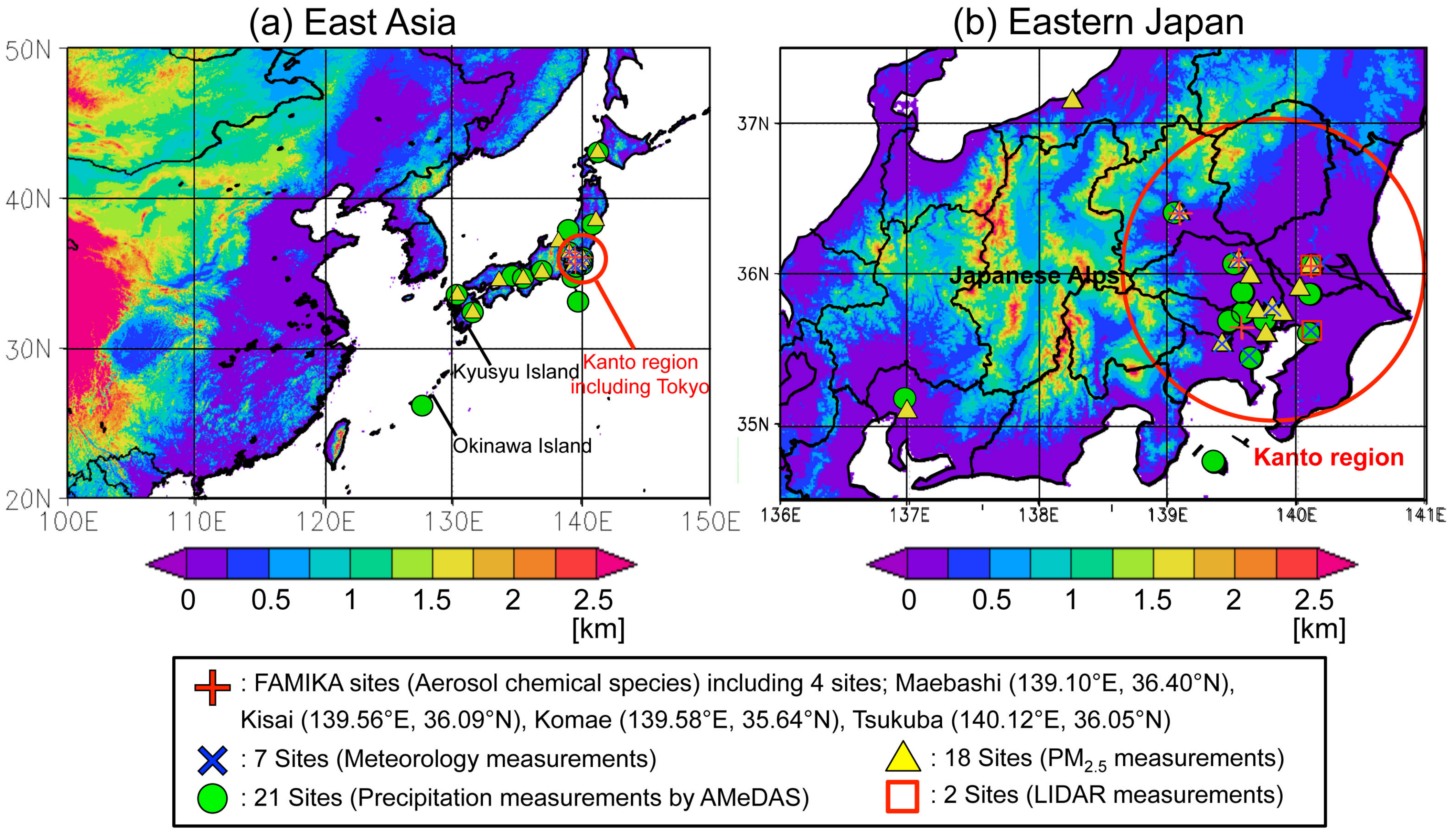
(a) East Asia
(b) Eastern Japan
50N
40N
30N
20N
100E
110E
120E
130E
140E
150E
Kyusyu Island
Okinawa Island
Kanto region
including Tokyo
37N
36N
35N
136E
137E
138E
139E
140E
141E
Japanese Alps
Kanto region
0
0.5
1
1.5
2
2.5
[km]
0
0.5
1
1.5
2
2.5
[km]
: FAMIKA sites (Aerosol chemical species) including 4 sites; Maebashi (139.10°E, 36.40°N),
Kisai (139.56°E, 36.09°N), Komae (139.58°E, 35.64°N), Tsukuba (140.12°E, 36.05°N)
: 7 Sites (Meteorology measurements)
: 21 Sites (Precipitation measurements by AMeDAS)
: 18 Sites ($PM_{2.5}$ measurements)
: 2 Sites (LIDAR measurements)

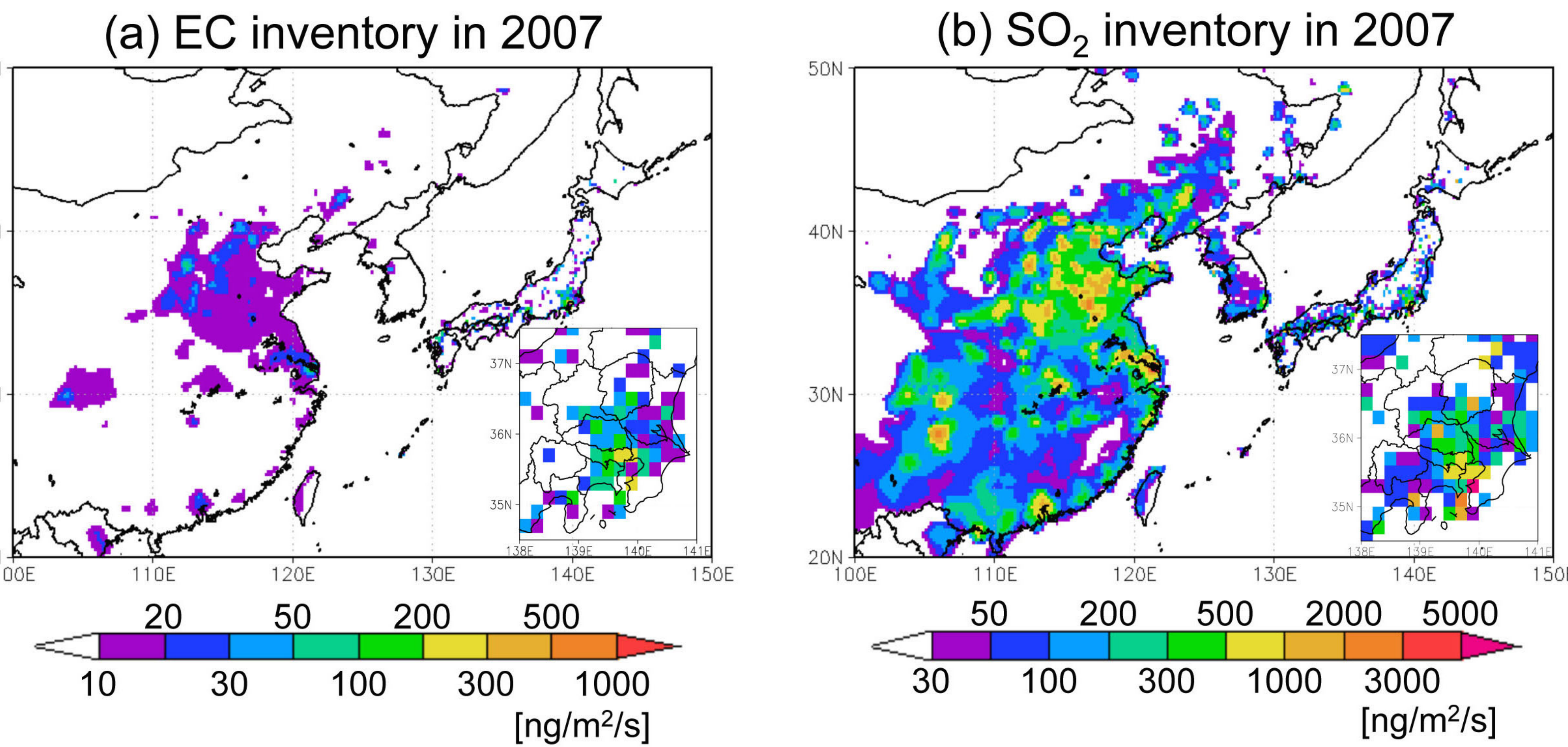
(a) EC inventory in 2007
50N
40N
30N
20N
100E
110E
120E
130E
140E
150E
37N
36N
35N
138E
139E
140E
141E
10
20
30
50
100
200
300
500
1000
[ng/m²/s]
(b) SO₂ inventory in 2007
30
50
100
200
300
500
1000
2000
3000
5000
[ng/m²/s]

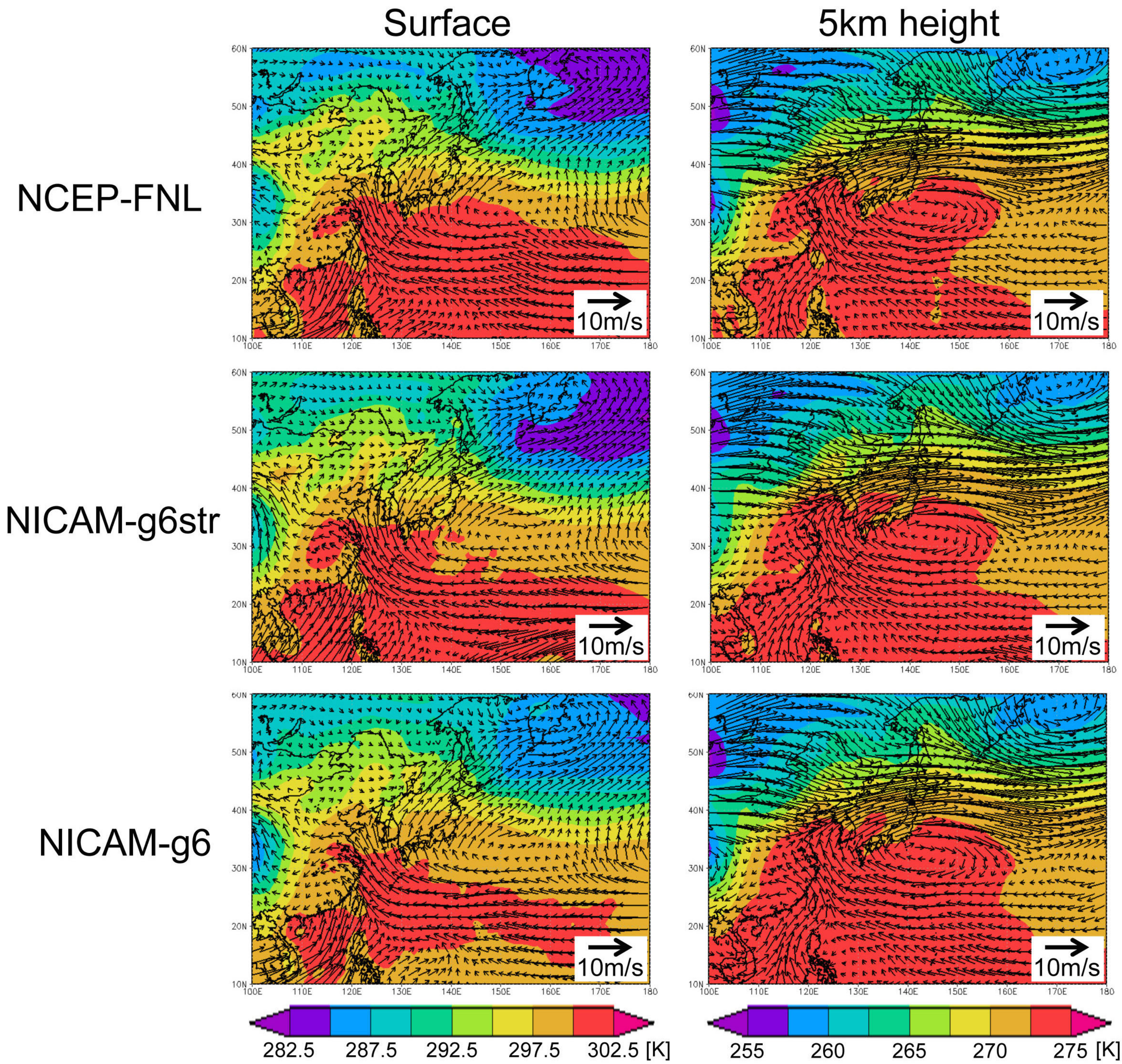

Surface
5km height
NCEP-FNL
NICAM-g6str
NICAM-g6
10m/s
282.5
287.5
292.5
297.5
302.5 [K]
255
260
265
270
275 [K]

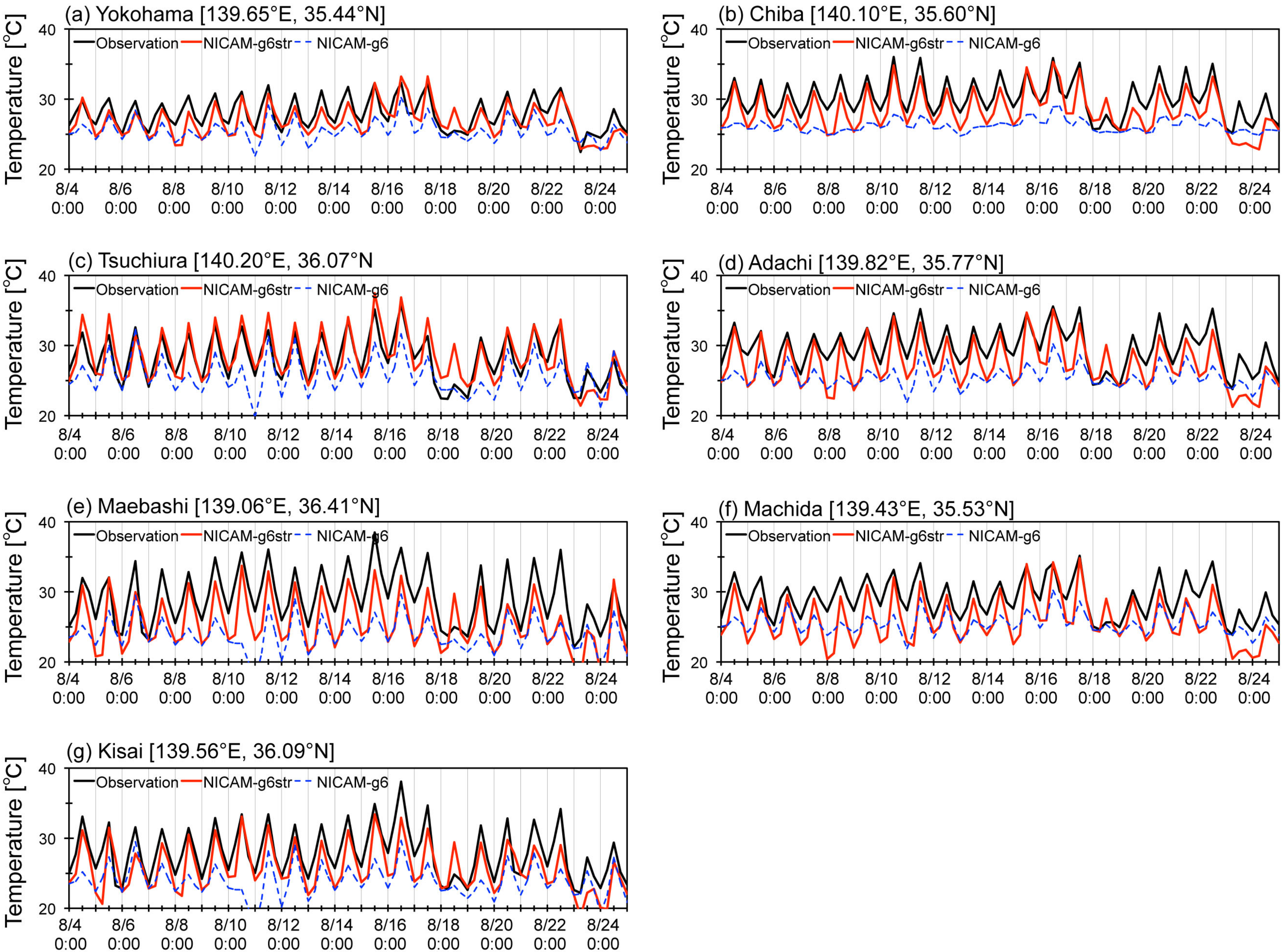
(a) Yokohama [139.65°E, 35.44°N]
(b) Chiba [140.10°E, 35.60°N]
(c) Tsuchiura [140.20°E, 36.07°N
(d) Adachi [139.82°E, 35.77°N]
(e) Maebashi [139.06°E, 36.41°N]
(f) Machida [139.43°E, 35.53°N]
(g) Kisai [139.56°E, 36.09°N]
Observation
NICAM-g6str
NICAM-g6
Temperature [°C]
20
30
40
8/4 0:00
8/6 0:00
8/8 0:00
8/10 0:00
8/12 0:00
8/14 0:00
8/16 0:00
8/18 0:00
8/20 0:00
8/22 0:00
8/24 0:00

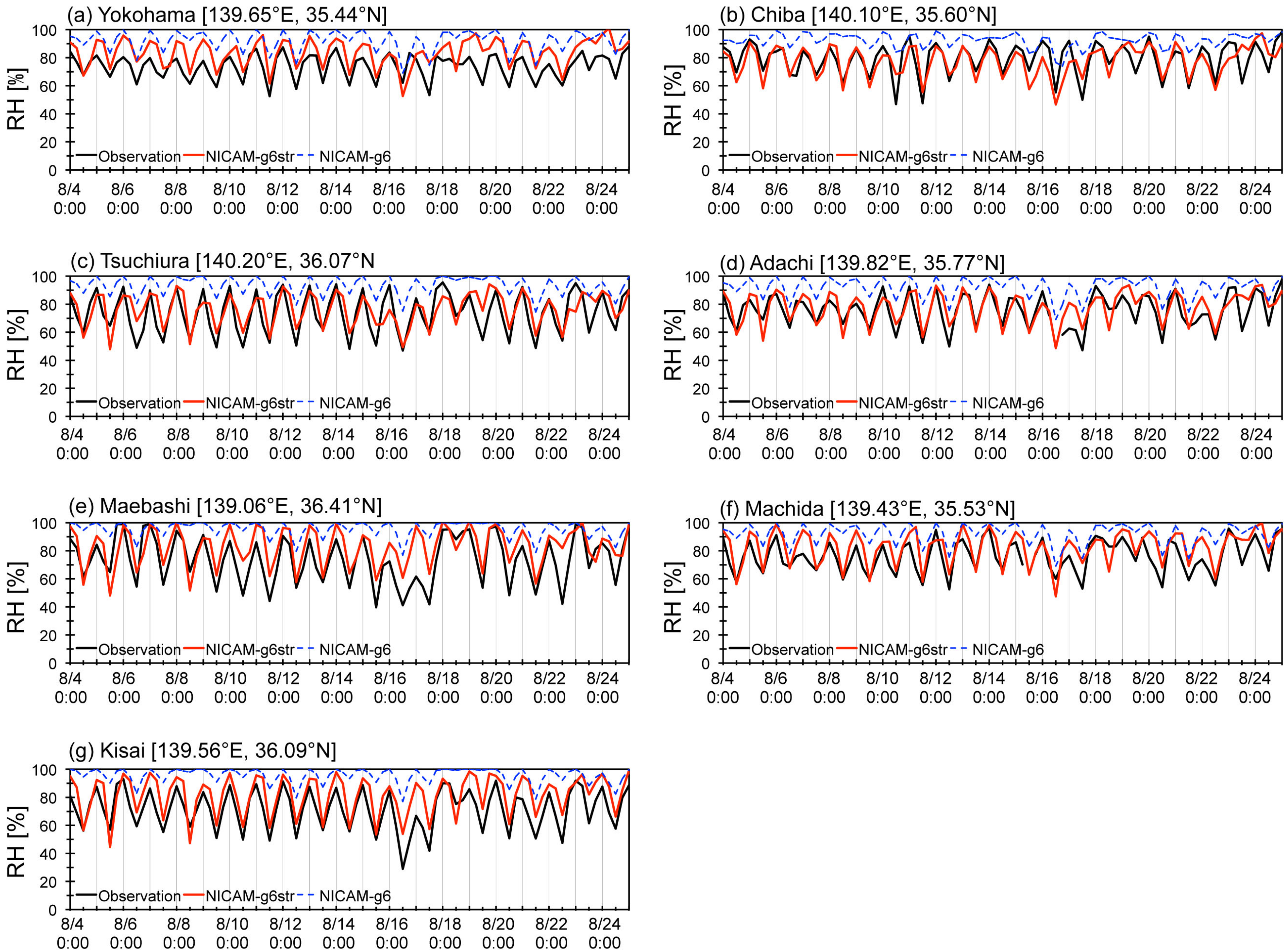

(a) Yokohama [139.65°E, 35.44°N]
(b) Chiba [140.10°E, 35.60°N]
(c) Tsuchiura [140.20°E, 36.07°N]
(d) Adachi [139.82°E, 35.77°N]
(e) Maebashi [139.06°E, 36.41°N]
(f) Machida [139.43°E, 35.53°N]
(g) Kisai [139.56°E, 36.09°N]
RH [%]
Observation
NICAM-g6str
NICAM-g6
8/4 0:00
8/6 0:00
8/8 0:00
8/10 0:00
8/12 0:00
8/14 0:00
8/16 0:00
8/18 0:00
8/20 0:00
8/22 0:00
8/24 0:00

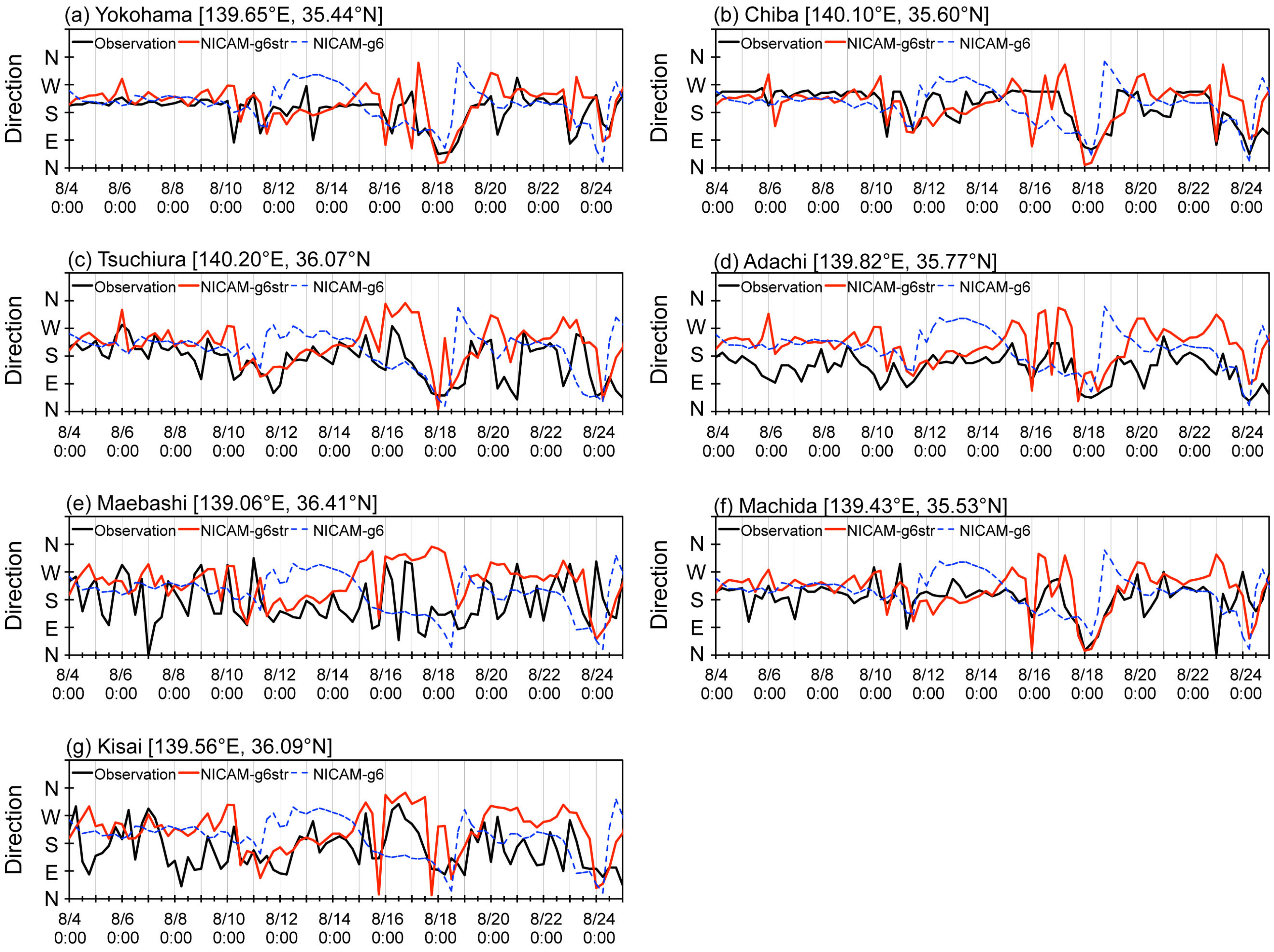
(a) Yokohama [139.65°E, 35.44°N]
(b) Chiba [140.10°E, 35.60°N]
(c) Tsuchiura [140.20°E, 36.07°N]
(d) Adachi [139.82°E, 35.77°N]
(e) Maebashi [139.06°E, 36.41°N]
(f) Machida [139.43°E, 35.53°N]
(g) Kisai [139.56°E, 36.09°N]
Observation
NICAM-g6str
NICAM-g6
Direction
N
W
S
E
N
8/4 0:00
8/6 0:00
8/8 0:00
8/10 0:00
8/12 0:00
8/14 0:00
8/16 0:00
8/18 0:00
8/20 0:00
8/22 0:00
8/24 0:00

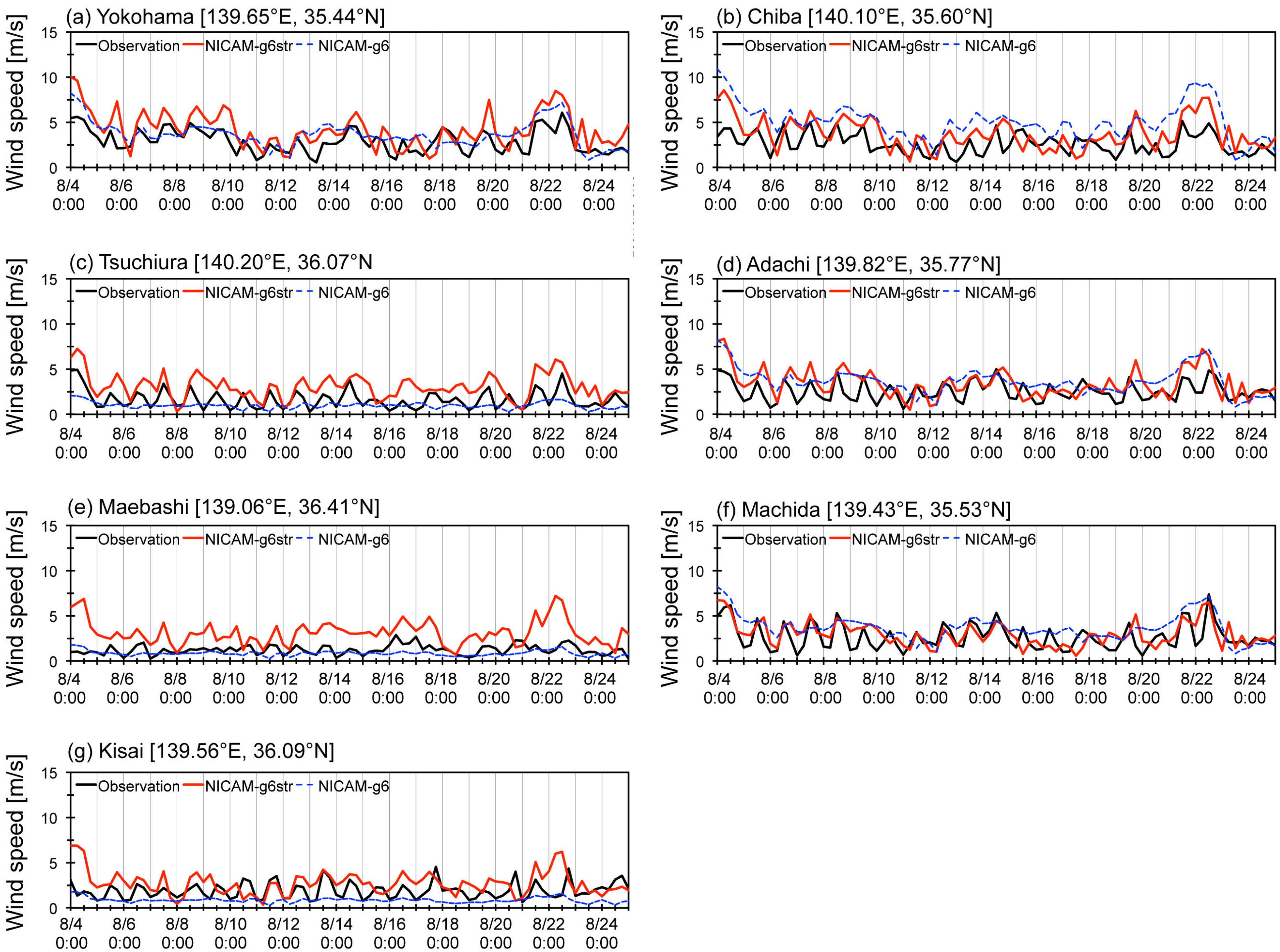
(a) Yokohama [139.65°E, 35.44°N]
(b) Chiba [140.10°E, 35.60°N]
(c) Tsuchiura [140.20°E, 36.07°N]
(d) Adachi [139.82°E, 35.77°N]
(e) Maebashi [139.06°E, 36.41°N]
(f) Machida [139.43°E, 35.53°N]
(g) Kisai [139.56°E, 36.09°N]
Observation
NICAM-g6str
NICAM-g6
Wind speed [m/s]
0
5
10
15
8/4 0:00
8/6 0:00
8/8 0:00
8/10 0:00
8/12 0:00
8/14 0:00
8/16 0:00
8/18 0:00
8/20 0:00
8/22 0:00
8/24 0:00

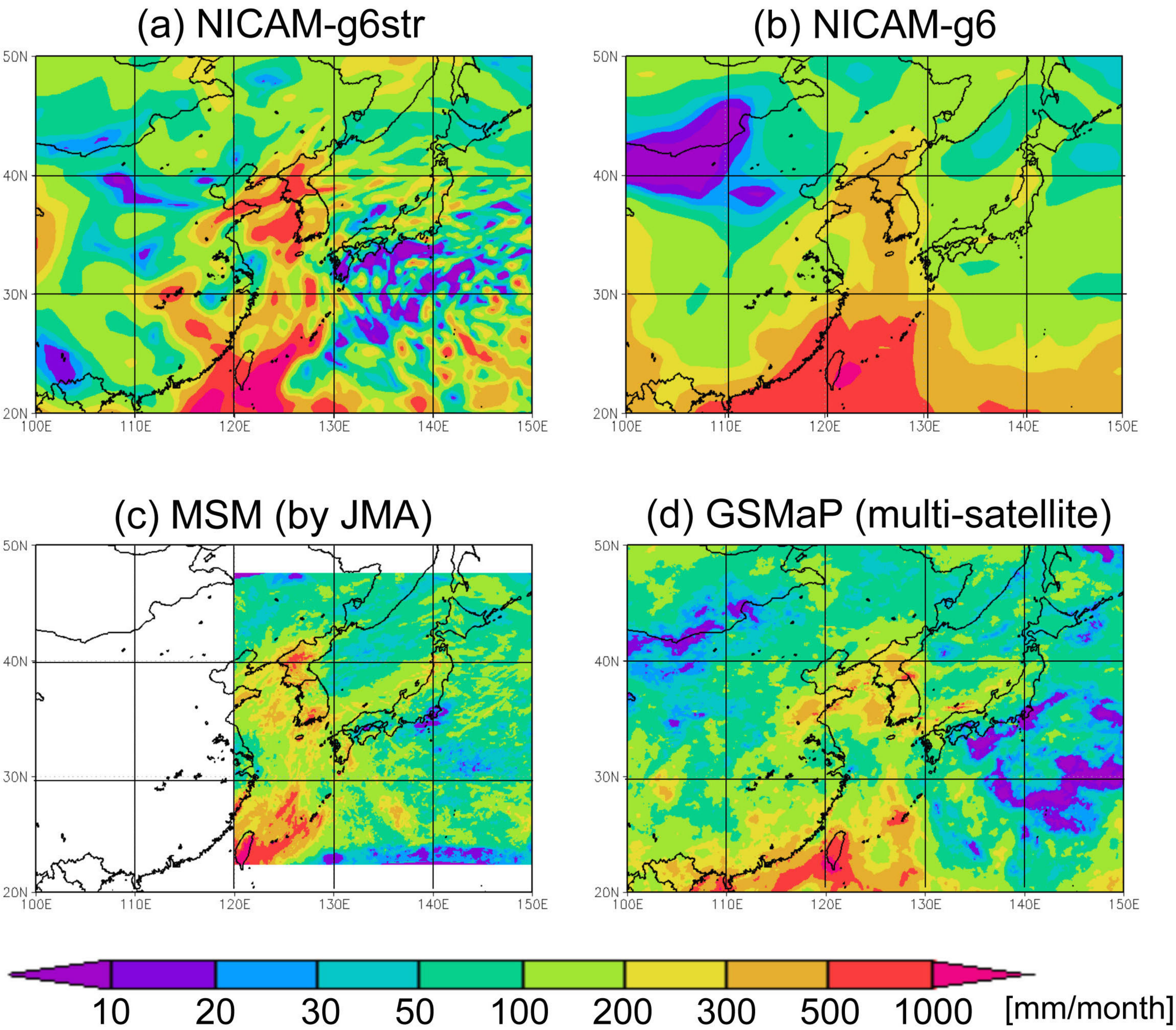
(a) NICAM-g6str
(b) NICAM-g6
(c) MSM (by JMA)
(d) GSMaP (multi-satellite)
50N
40N
30N
20N
100E
110E
120E
130E
140E
150E
10
20
30
50
100
200
300
500
1000
[mm/month]

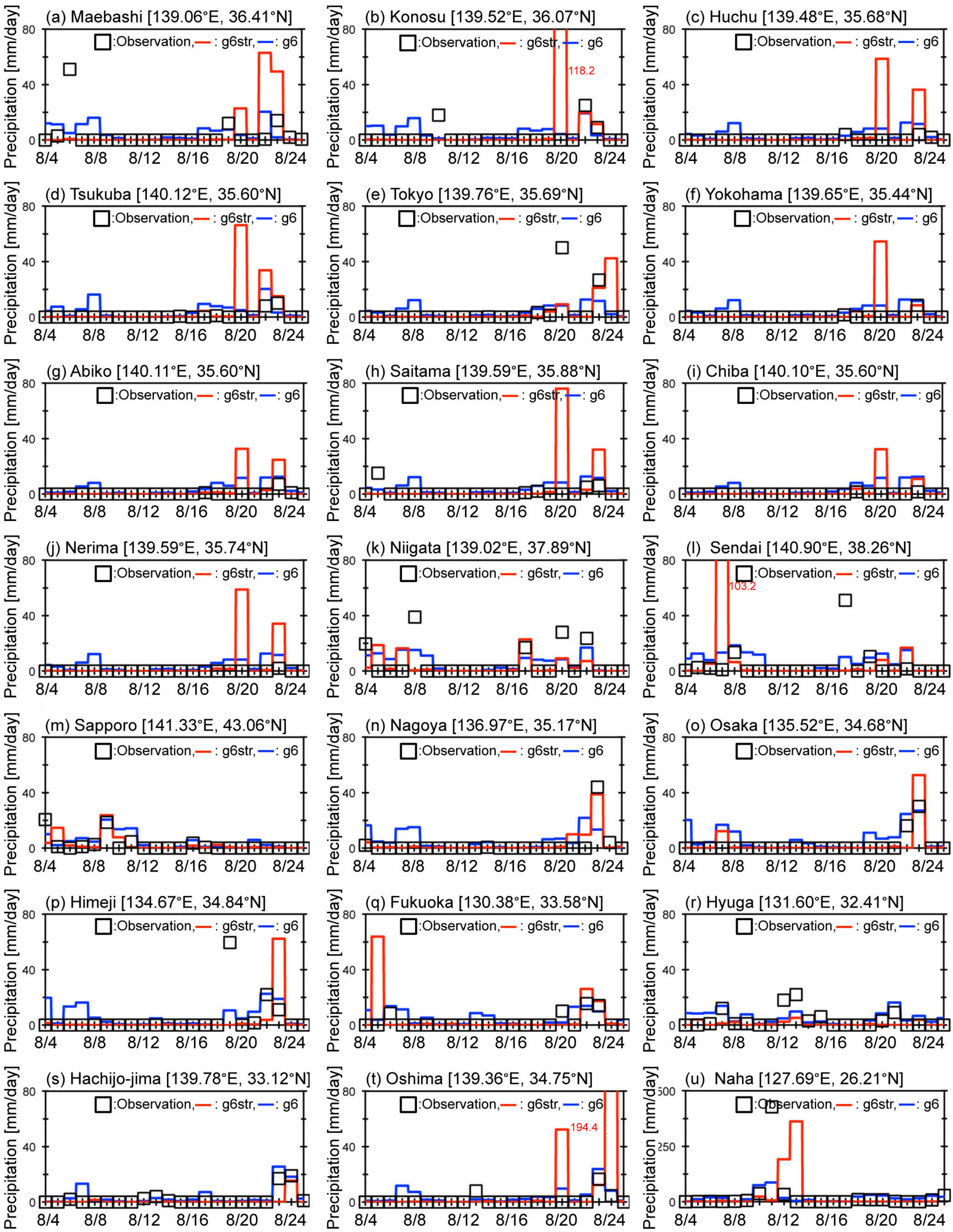

(a) Maebashi [139.06°E, 36.41°N]
(b) Konosu [139.52°E, 36.07°N]
118.2
(c) Huchu [139.48°E, 35.68°N]
(d) Tsukuba [140.12°E, 35.60°N]
(e) Tokyo [139.76°E, 35.69°N]
(f) Yokohama [139.65°E, 35.44°N]
(g) Abiko [140.11°E, 35.60°N]
(h) Saitama [139.59°E, 35.88°N]
(i) Chiba [140.10°E, 35.60°N]
(j) Nerima [139.59°E, 35.74°N]
(k) Niigata [139.02°E, 37.89°N]
(l) Sendai [140.90°E, 38.26°N]
103.2
(m) Sapporo [141.33°E, 43.06°N]
(n) Nagoya [136.97°E, 35.17°N]
(o) Osaka [135.52°E, 34.68°N]
(p) Himeji [134.67°E, 34.84°N]
(q) Fukuoka [130.38°E, 33.58°N]
(r) Hyuga [131.60°E, 32.41°N]
(s) Hachijo-jima [139.78°E, 33.12°N]
(t) Oshima [139.36°E, 34.75°N]
194.4
(u) Naha [127.69°E, 26.21°N]
:Observation, : g6str, : g6
Precipitation [mm/day]
0
40
80
250
500
8/4
8/8
8/12
8/16
8/20
8/24

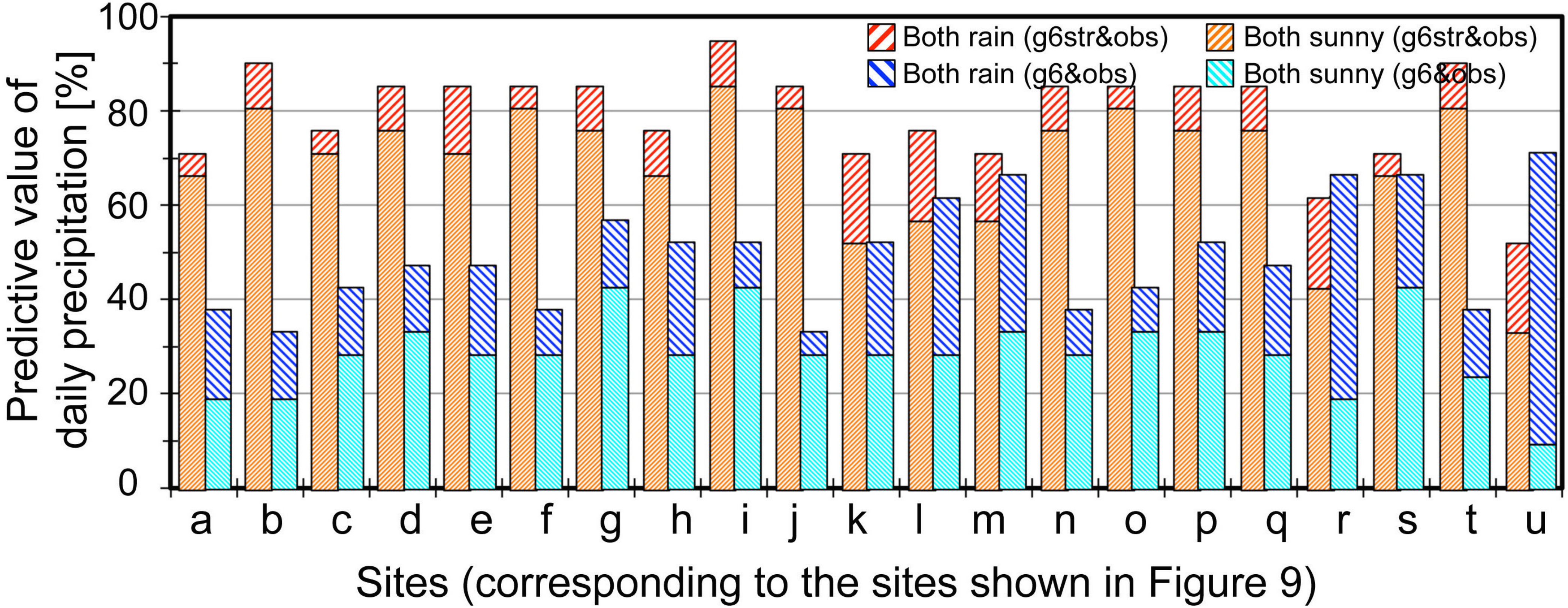
Both rain (g6str&obs)
Both sunny (g6str&obs)
Both rain (g6&obs)
Both sunny (g6&obs)
Predictive value of daily precipitation [%]
0
20
40
60
80
100
a
b
c
d
e
f
g
h
i
j
k
l
m
n
o
p
q
r
s
t
u
Sites (corresponding to the sites shown in Figure 9)

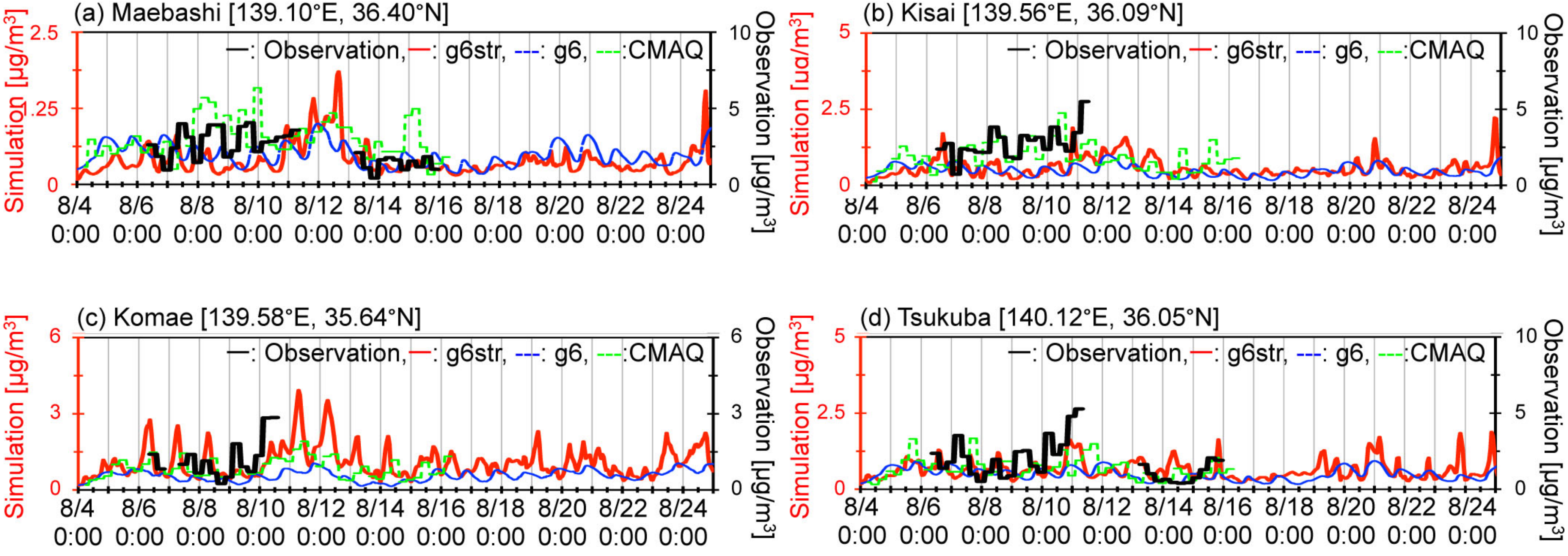

(a) Maebashi [139.10°E, 36.40°N]
(b) Kisai [139.56°E, 36.09°N]
(c) Komae [139.58°E, 35.64°N]
(d) Tsukuba [140.12°E, 36.05°N]
—: Observation, —: g6str, ---: g6, ---:CMAQ
Simulation [μg/m³]
Observation [μg/m³]
8/4 0:00
8/6 0:00
8/8 0:00
8/10 0:00
8/12 0:00
8/14 0:00
8/16 0:00
8/18 0:00
8/20 0:00
8/22 0:00
8/24 0:00

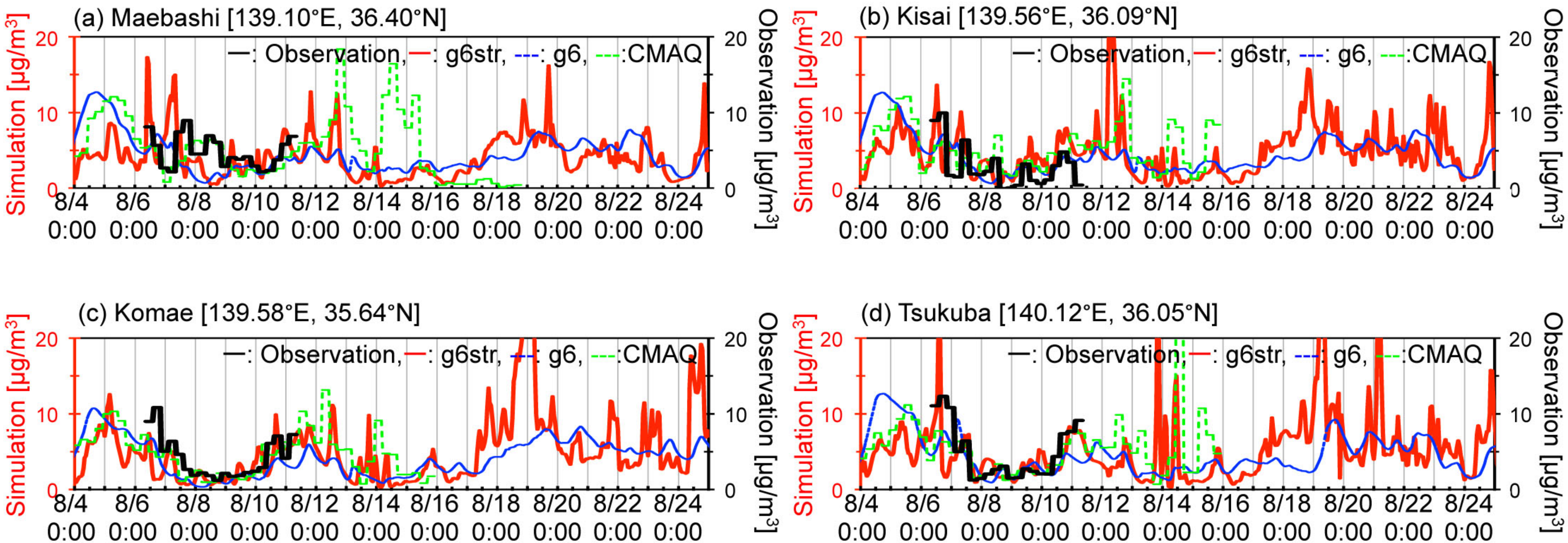
(a) Maebashi [139.10°E, 36.40°N]
(b) Kisai [139.56°E, 36.09°N]
(c) Komae [139.58°E, 35.64°N]
(d) Tsukuba [140.12°E, 36.05°N]
: Observation, : g6str, : g6, :CMAQ
Simulation [μg/m3]
Observation [μg/m3]
0
10
20
8/4 0:00
8/6 0:00
8/8 0:00
8/10 0:00
8/12 0:00
8/14 0:00
8/16 0:00
8/18 0:00
8/20 0:00
8/22 0:00
8/24 0:00

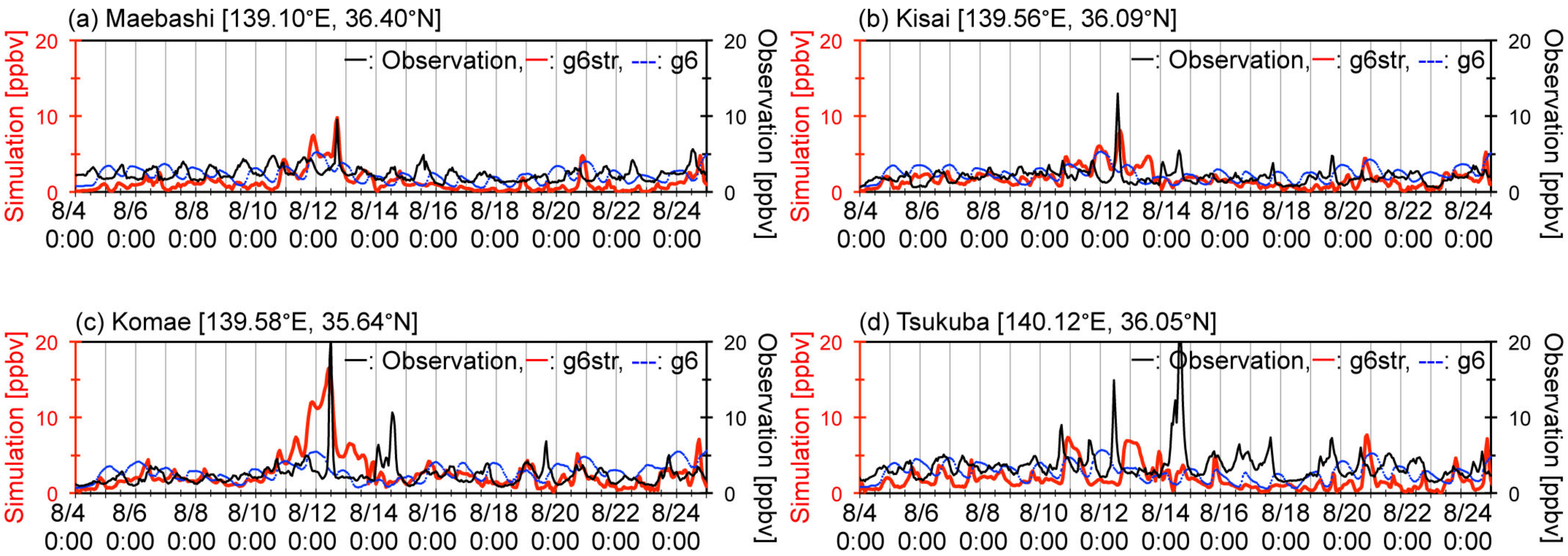

(a) Maebashi [139.10°E, 36.40°N]
(b) Kisai [139.56°E, 36.09°N]
(c) Komae [139.58°E, 35.64°N]
(d) Tsukuba [140.12°E, 36.05°N]
: Observation, : g6str, : g6
Simulation [ppbv]
Observation [ppbv]
0
10
20
8/4 0:00
8/6 0:00
8/8 0:00
8/10 0:00
8/12 0:00
8/14 0:00
8/16 0:00
8/18 0:00
8/20 0:00
8/22 0:00
8/24 0:00

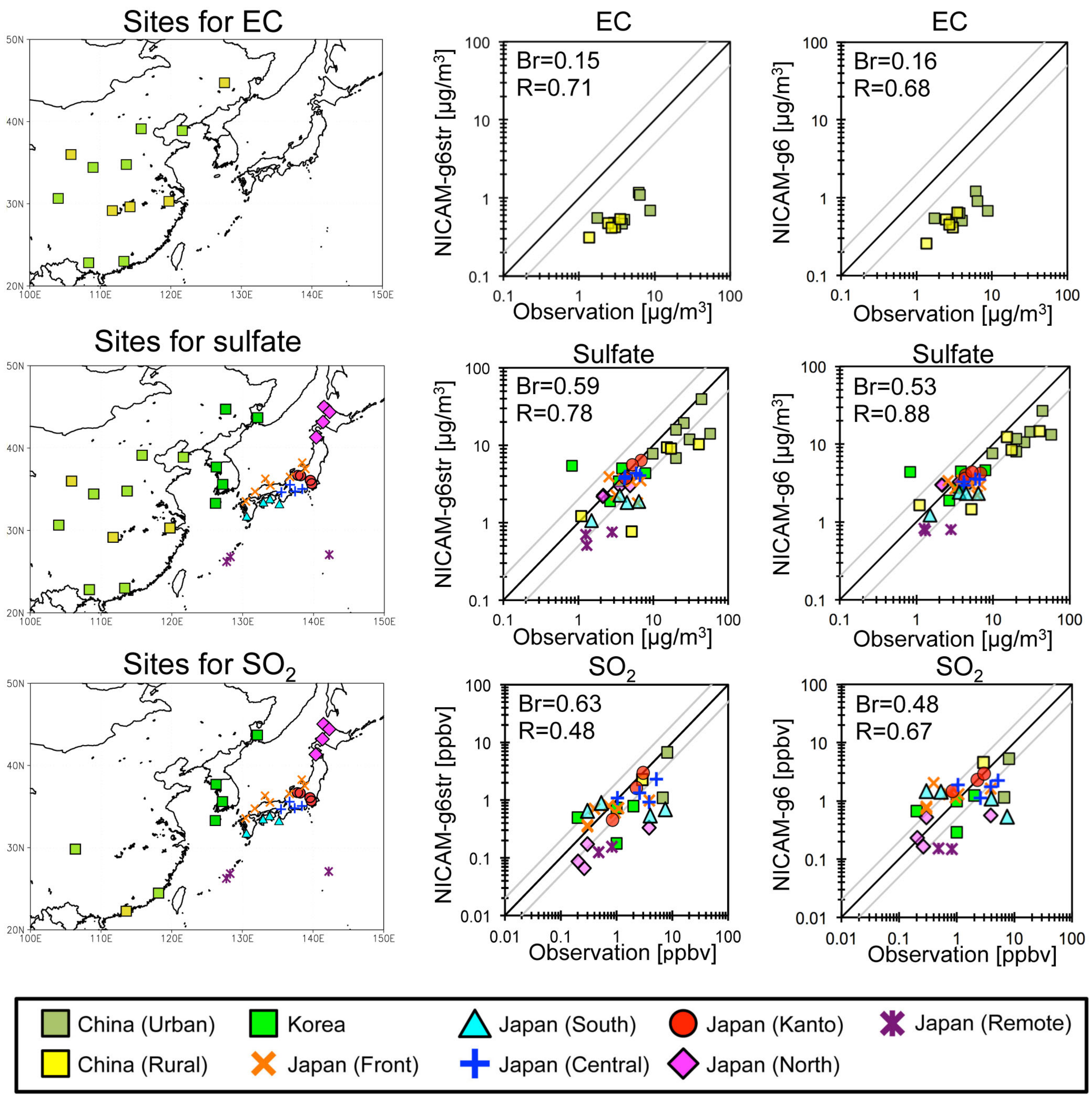

Sites for EC
EC
Br=0.15
R=0.71
NICAM-g6str [μg/m^3]
Observation [μg/m^3]
EC
Br=0.16
R=0.68
NICAM-g6 [μg/m^3]
Observation [μg/m^3]
Sites for sulfate
Sulfate
Br=0.59
R=0.78
Sulfate
Br=0.53
R=0.88
Sites for SO_2
SO_2
Br=0.63
R=0.48
NICAM-g6str [ppbv]
Observation [ppbv]
SO_2
Br=0.48
R=0.67
NICAM-g6 [ppbv]
China (Urban)
China (Rural)
Korea
Japan (Front)
Japan (South)
Japan (Central)
Japan (Kanto)
Japan (North)
Japan (Remote)

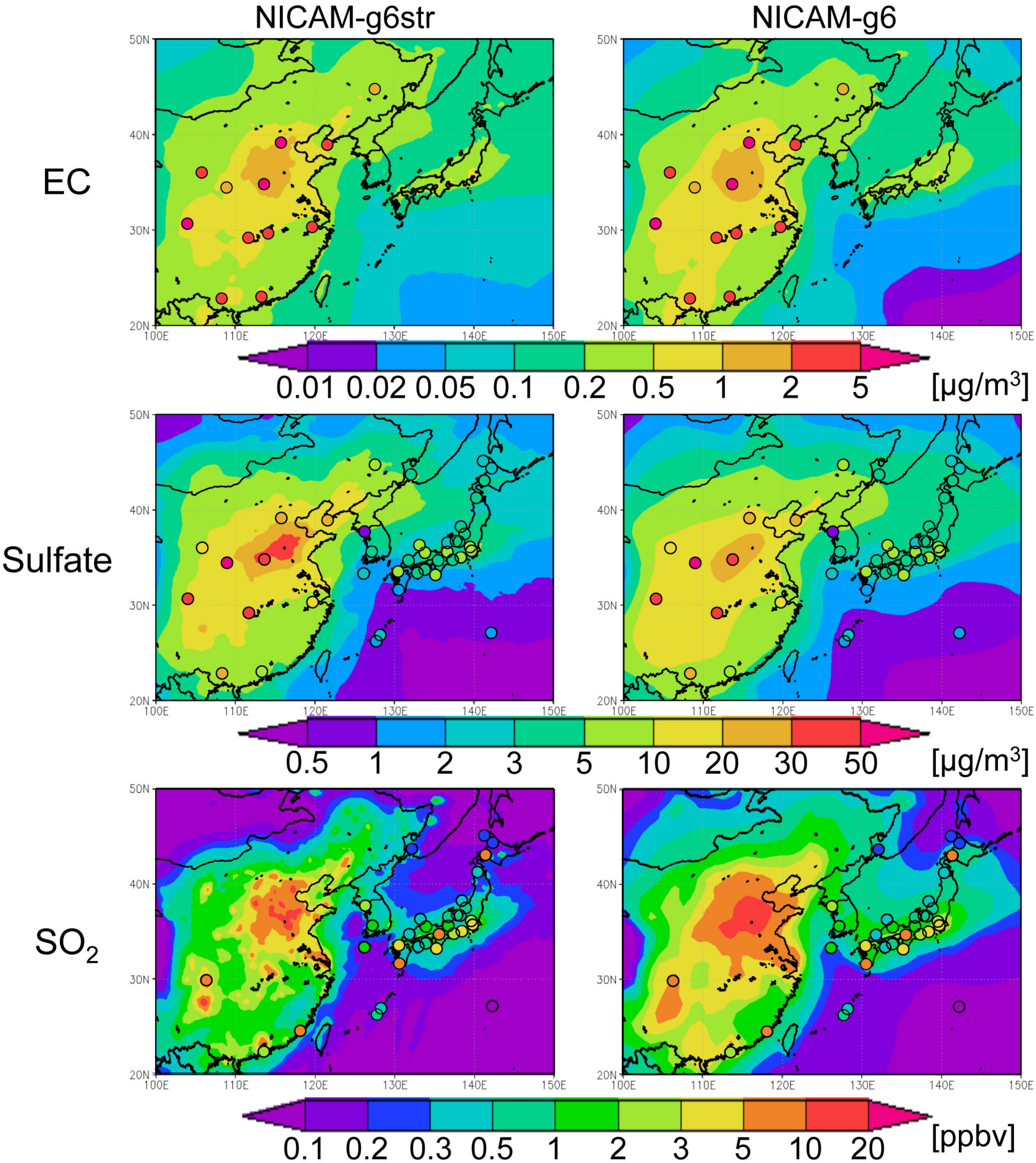

NICAM-g6str
NICAM-g6
EC
Sulfate
SO2
50N
40N
30N
20N
100E
110E
120E
130E
140E
150E
0.01 0.02 0.05 0.1 0.2 0.5 1 2 5
[μg/m3]
0.5 1 2 3 5 10 20 30 50
[μg/m3]
0.1 0.2 0.3 0.5 1 2 3 5 10 20
[ppbv]

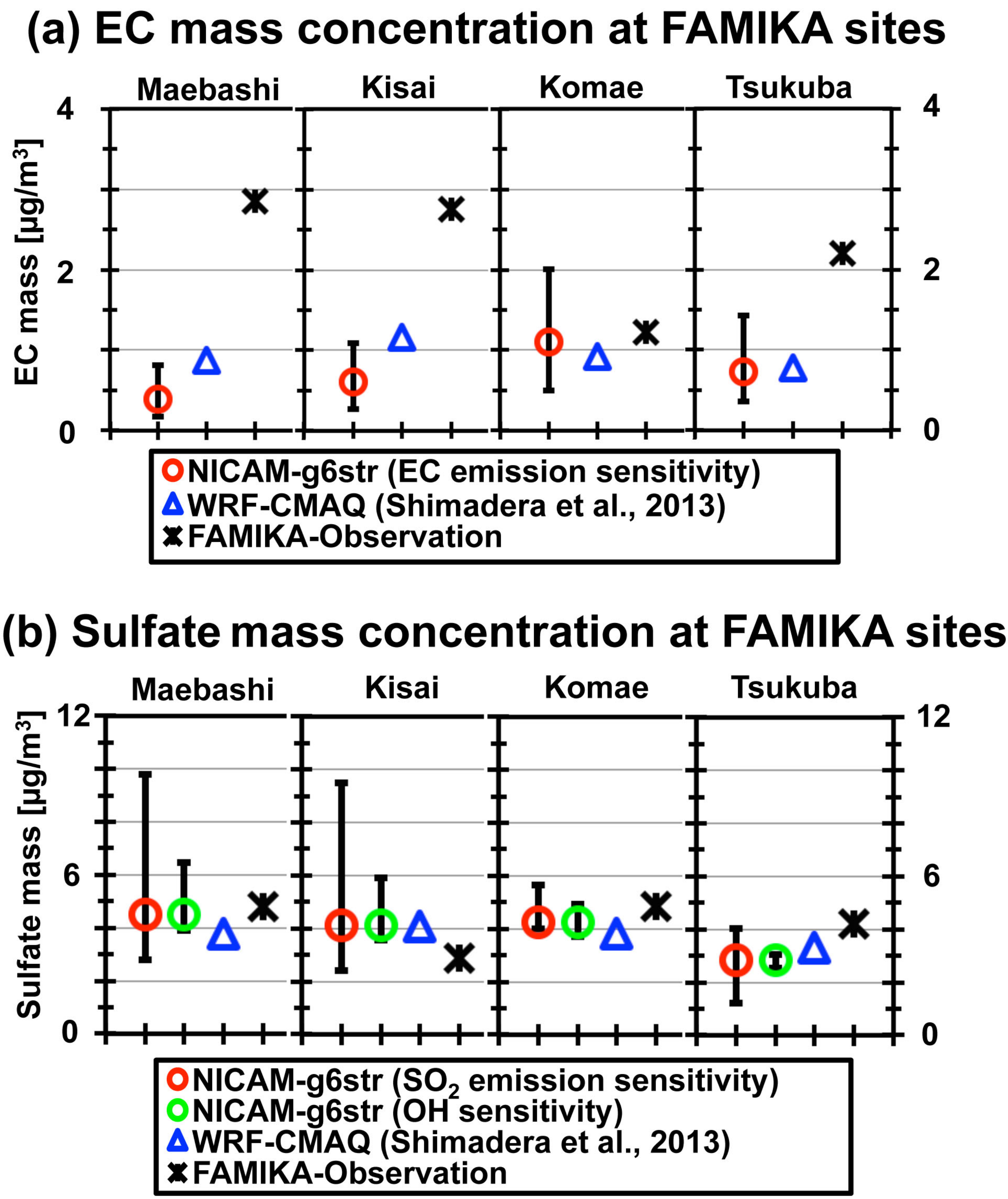
(a) EC mass concentration at FAMIKA sites
Maebashi
Kisai
Komae
Tsukuba
EC mass [μg/m³]
0
2
4
NICAM-g6str (EC emission sensitivity)
WRF-CMAQ (Shimadera et al., 2013)
FAMIKA-Observation
(b) Sulfate mass concentration at FAMIKA sites
Maebashi
Kisai
Komae
Tsukuba
Sulfate mass [μg/m³]
0
6
12
NICAM-g6str (SO2 emission sensitivity)
NICAM-g6str (OH sensitivity)
WRF-CMAQ (Shimadera et al., 2013)
FAMIKA-Observation

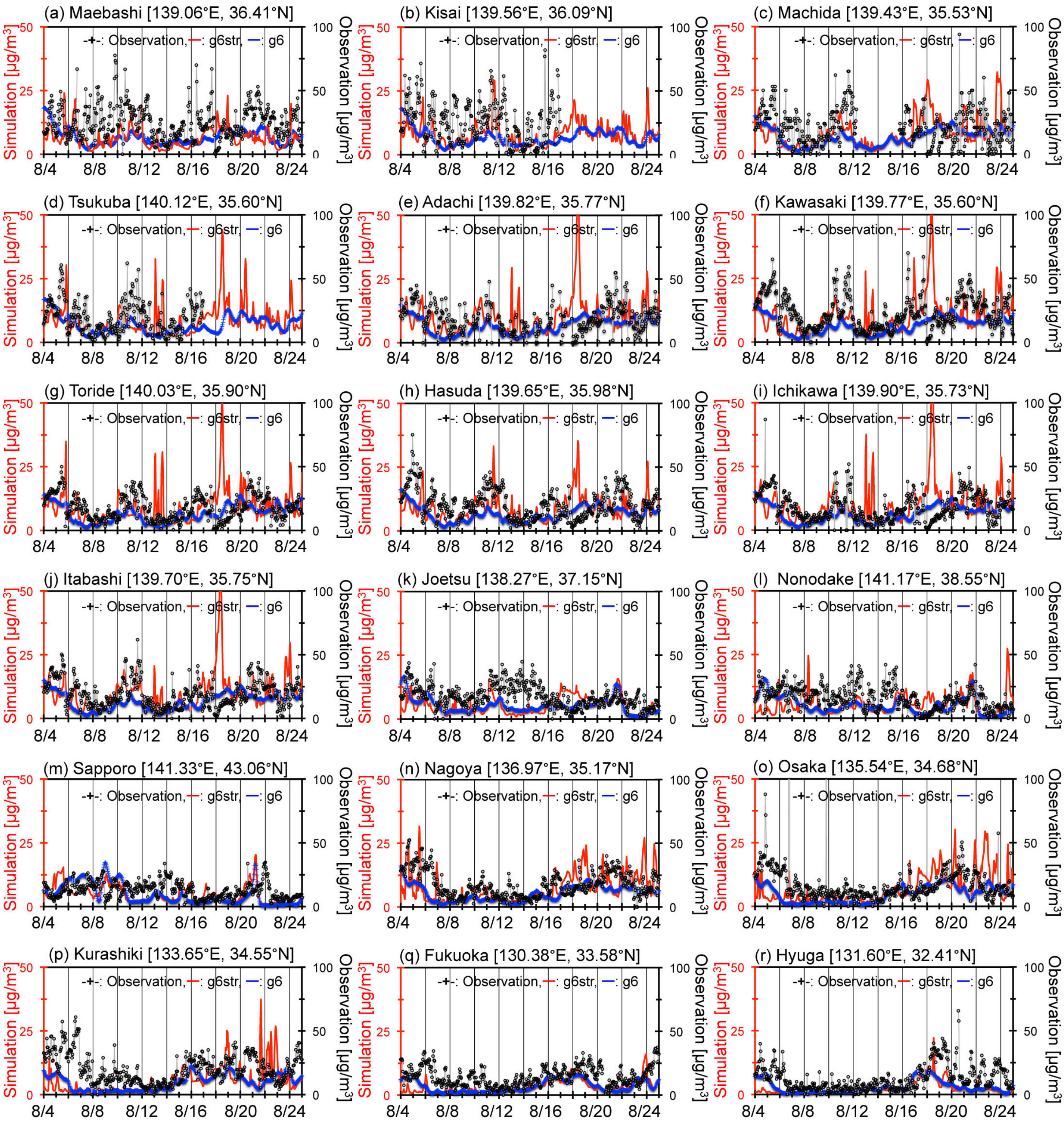
(a) Maebashi [139.06°E, 36.41°N]
(b) Kisai [139.56°E, 36.09°N]
(c) Machida [139.43°E, 35.53°N]
(d) Tsukuba [140.12°E, 35.60°N]
(e) Adachi [139.82°E, 35.77°N]
(f) Kawasaki [139.77°E, 35.60°N]
(g) Toride [140.03°E, 35.90°N]
(h) Hasuda [139.65°E, 35.98°N]
(i) Ichikawa [139.90°E, 35.73°N]
(j) Itabashi [139.70°E, 35.75°N]
(k) Joetsu [138.27°E, 37.15°N]
(l) Nonodake [141.17°E, 38.55°N]
(m) Sapporo [141.33°E, 43.06°N]
(n) Nagoya [136.97°E, 35.17°N]
(o) Osaka [135.54°E, 34.68°N]
(p) Kurashiki [133.65°E, 34.55°N]
(q) Fukuoka [130.38°E, 33.58°N]
(r) Hyuga [131.60°E, 32.41°N]
-+-: Observation, –: g6str, –: g6
Simulation [µg/m3]
Observation [µg/m3]
8/4 8/8 8/12 8/16 8/20 8/24

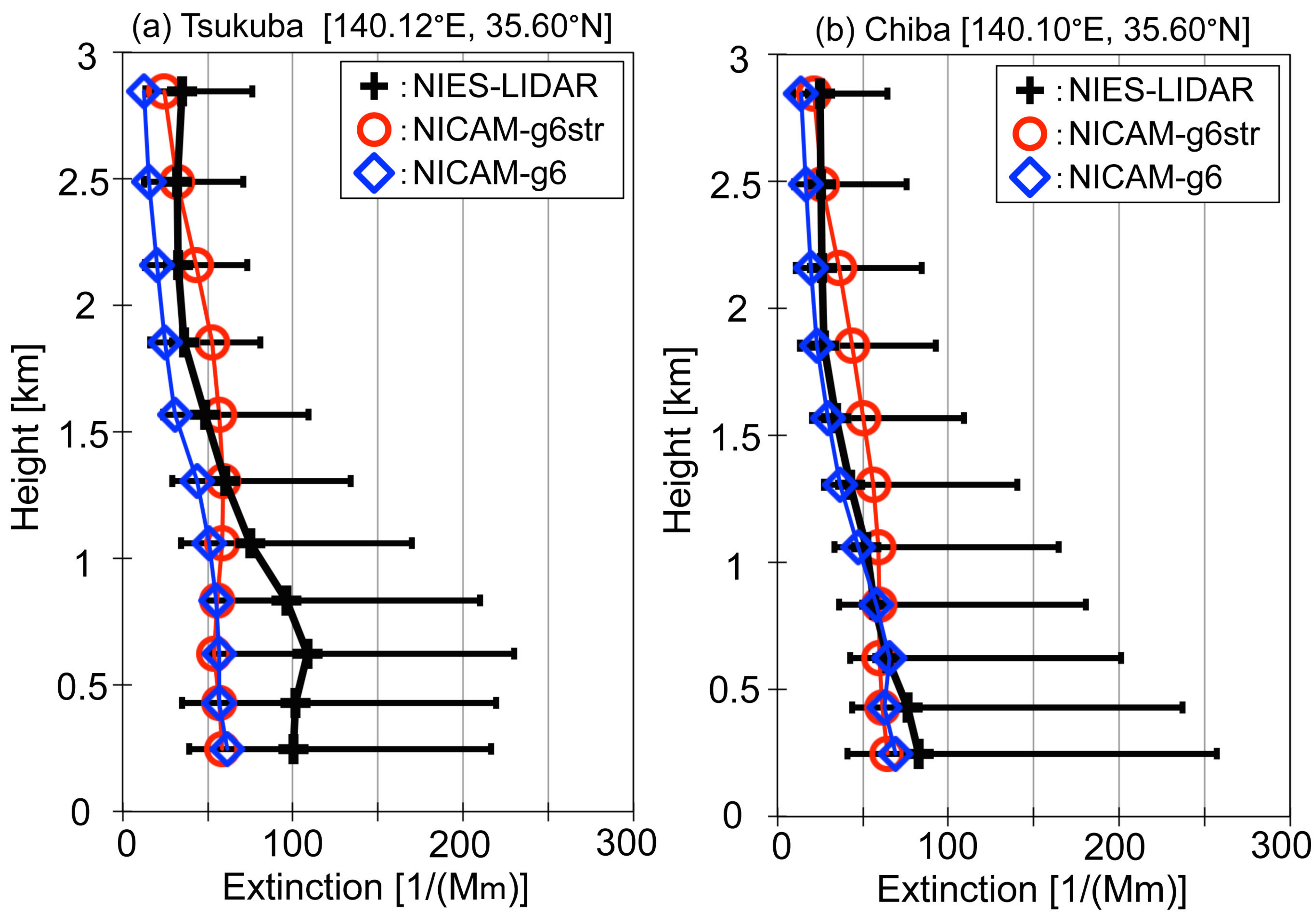

(a) Tsukuba [140.12°E, 35.60°N]
: NIES-LIDAR
: NICAM-g6str
: NICAM-g6
Height [km]
Extinction [1/(Mm)]
(b) Chiba [140.10°E, 35.60°N]
: NIES-LIDAR
: NICAM-g6str
: NICAM-g6
Height [km]
Extinction [1/(Mm)]